ISSN 2070-0482, Mathematical Models and Computer Simulations, 2024, Vol. 16, No. 1, pp. 123–155. © Pleiades Publishing, Ltd., 2024.
Russian Text © The Author(s), 2023, published in Matematicheskoe Modelirovanie, 2023, Vol. 35, No. 10, pp. 69–112.

Evaluation of the Accuracy of Modern Codes by Comparing the Calculated and Experimental Data on the Example of a Problem on a Supersonic Viscous Turbulent Gas Flow Around a Tandem of Back-Forcing and Forward-Forcing Steps

S. M. Bosnyakov[a,]*, M. E. Berezko[b], Yu. N. Deryugin[c], A. P. Duben[d], R. N. Zhuchkov[c], A. S. Kozelkov[c], T. K. Kozubskaya[d], S. V. Matyash[a], S. V. Mikhailov[a], M. K. Okulov[b], V. A. Talyzin[a], A. A. Utkina[c], N. A. Kharchenko[a], and V. I. Shevyakov[c]

[a] *Zhukovsky Central Aerohydrodynamic Institute, Zhukovsky, Moscow oblast, 140181 Russia*
[b] *Irkut Corporation Regional Aircraft Branch, Moscow, Russia*
[c] *Russian Federal Nuclear Center—All-Russian Research Institute of Experimental Physics, Sarov, Nizhny Novgorod oblast, Russia*
[d] *Keldysh Institute of Applied Mathematics, Russian Academy of Sciences, Moscow, Russia*
**e-mail: bosnyakov@tsagi.ru*

Received May 22, 2023; revised May 22, 2023; accepted September 11, 2023

Abstract—Various program codes for the investigation of a viscous turbulent compressible gas flow around complicated configurations are described. A series of test calculations for a tandem of 3D back-forcing and forward-forcing steps are performed. The purpose of the calculations is to analyze the resolution accuracy of the separation zones using classical and modern methods. To achieve the goal, the physical features of the flow are described and the results obtained using different codes in the back-forcing and forward-forcing steps tandem test case are compared.

Keywords: supersonic flow, RANS, LES, IDDES, tandem of steps, rarefaction, compression, return flow, shock, separation point, attachment point, comparison of numerical and experimental results, accuracy

DOI: 10.1134/S2070048224010046

1. INTRODUCTION

In the Zhukovsky Central Aerohydrodynamic Institute (TsAGI)—Russian Academy of Sciences (RAS) cooperation program, the Khristianovich Institute of Theoretical and Applied Mechanics, Siberian Branch, Russian Academy of Sciences (ITAM SB RAS) obtained and systematized reliable experimental data [1] on the flow of a supersonic turbulent gas flow around a model configuration of a tandem of 3D back-forcing and forward-forcing steps. The specified data was transferred to TsAGI in the form of a report with primary and secondary documentation. Partial data from the report was published in [2].

The problem of the flow around a tandem of steps, consisting of 3D back-forcing and forward-forcing steps, is relevant and has aroused the interest of various groups of scientists. The physical features of the flow arising behind the step were studied in detail in [1–3]. In this case, the calculation in [2] was performed using the RANS and LES methods, and the calculation in [3] was performed using the DNS method. Not only the qualitative but also the quantitative agreement between the calculated and experimental data is shown. The appearance of regular structures such as longitudinal Görtler vortices was noted. The return flow zone (separation), as well as compression and rarefaction waves, were studied in detail.

At the CEAA 2022 conference in Svetlogorsk, a special session was organized at which representatives of several organizations (TsAGI, Keldysh Institute of Applied Mathematics (IAM), Russian Federal Nuclear Center—All-Russian Research Institute of Experimental Physics (RFNC-VNIIEF), and Irkut Corporation Regional Aircraft Branch) presented and discussed the results of testing the program codes

Table 1. Coordinates of flow separation and attachment points

Experiment	X	Y
Separation S	$0.1\,h$	$0.9\,h$
Attachment R	$1.85\,h$	$-1.0\,h$

they use based on a test prepared for a tandem step with a base depression angle of 45° (BFS 45). The session's organizers constructed two grids (structured and unstructured) and offered them to the participants, but the use of these grids was not mandatory due to the differences in the structures of the programs being tested. As an exception, it was allowed to use one's own topologically similar grids with the number of cells approximately equal to the given one. This condition was only partially met.

2. PHYSICAL FEATURES OF THE FLOW BEHIND A RETURN STEP

In a supersonic flow around the considered tandem of steps, in accordance with [1], a complex flow pattern is formed. From the rarefaction angle, a rarefaction wave fan (RWF) propagates into the external flow; see Fig. 1, in which the flow is rotated by an angle of –45°. This is followed by shock wave 2 from the compression step with an angle of 45°, in which the flow returns to the original direction. The specified shock wave leads to the formation of a separation, which creates a separation step, generating an additional separation shock wave 1. Thus, the separated flow in the vicinity of a tandem of steps resembles the flow that arises under the influence of a shock wave in the compression angle in front of an inclined step oriented against the flow, which was numerically simulated in [4].

Within the separation zone, areas of forward-forcing and return-forcing flow can be distinguished. The zero-velocity line in Fig. 2 is marked by a dotted line with diamonds, which correspond to the position of the experimental points obtained by constructing the velocity profiles in the experiment [1]. The coordinates of the flow separation and attachment points in the step symmetry plane are given in Table 1.

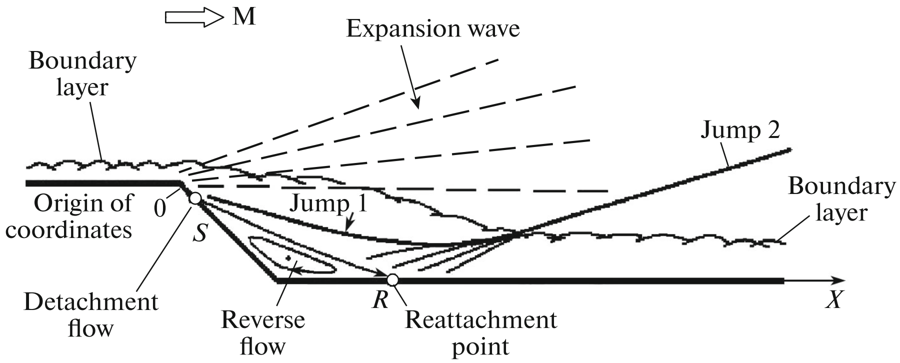

Fig. 1. Flow diagram around a tandem of steps.

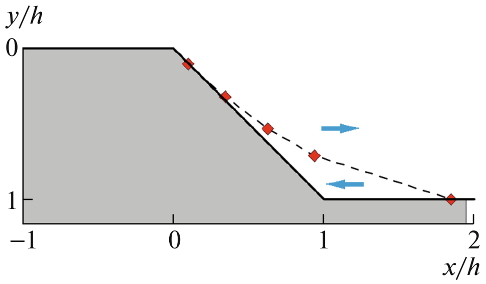

Fig. 2. Zero velocity line separating forward and return flows.

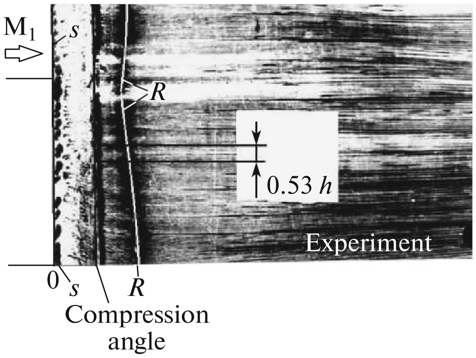

Fig. 3. Photograph of the limiting streamlines on the surface of the step in the experiment.

In a spatial flow, the lines of flow separation and attachment have a curvilinear shape. This is clearly visible in the photograph (see Fig. 3) of the limiting current lines recorded in the experiment using soot-oil visualization. Letter *S* marks the line of separation (flow) on the inclined face behind the top of the ledge; and letter *R*, the line of attachment (spreading). The photograph also shows the characteristic longitudinal lines of the flow and spreading along the width of the model, which are associated with the emerging longitudinal periodic vortex structures (Görtler vortices). The measurements provide an estimate for the characteristic size of the noted vortex structures of $D = 0.53h$. This size is used for further comparisons of the calculated and experimental results. Nevertheless, it should be noted that all the data on Görtler vortices are approximate and require further clarification.

3. EXPERIMENTAL MODEL AND FEATURES OF THE EXPERIMENT AT THE KHRISTIANOVICH ITAM SB RAS

The experimental model [1] (see Fig. 4) comprised rectangular parallel plates (*1* and *3*) 400 mm wide, forming a straight ledge with a height of h = 15 mm at a distance of 315 mm from the leading edge of the plate. The total length of the model is 585 mm. An inclined surface of the ledge is implemented using liner *2* with the angle of deflection of the leeward edge of −45°.

The model is installed horizontally on a vertical pylon located in the working part of the supersonic wind tunnel (SWT) T-313 ITAM SB RAS [5]. In this case, the position of the surface of plate *1* corresponded to the horizontal plane of symmetry of the working part of the wind tunnel. The surfaces of plate *1*, liner *2*, and back plate *3* were drained. Drainage holes with a diameter of 0.5 mm were located in the vicinity of the plane of symmetry of the model with a variable step ranging from 1 to 5 mm. To exclude the influence of the laminar-turbulent transition in the boundary layer on the studied flow, a wire turbu-

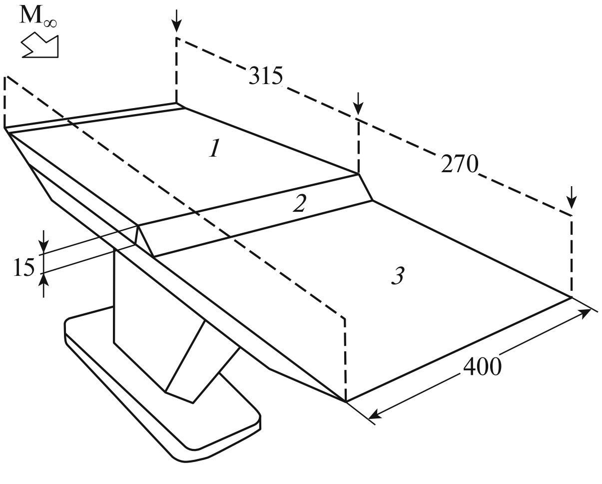

Fig. 4. Scheme of the experimental model [1].

Table 2. Free flow parameters

Model	M_∞	p_0, kPa	p_∞, kPa	T_0, K	$Re_l \times 10^{-6}$, m^{-1}
BFS 45	3.01 ± 0.005	419.7 ± 2	11.2 ± 0.1	292 ± 0.4	32.7 ± 0.7

lator with a diameter of 0.5 mm was located on the surface of plate *1* at a distance of 3 mm from its leading edge. Measurements of the total pressure profiles in the undisturbed boundary layer in front of the step, in the separation zone, and further downstream were carried out in the vicinity of the vertical plane of symmetry of the model using the appropriate miniature pneumatic probes. The probes were moved vertically in the direction from the model surface using a coordinate controller. The minimum step and accuracy of their movement vertically was 0.1 mm; and horizontally, 0.5 mm. The moment of contact of the pneumatic probes with the surface was controlled using an electrical contact. All probes were made of medical needles with a small diameter of 0.87 mm and mounted on thin fairings with a sharp (thickness 0.02–0.05 mm) leading edge. The entrance hole was flattened and had a height of 0.1 mm. For measurements in the region of the return flow in the separation zone, an appropriate probe was used, oriented towards this flow.

Table 2 shows the nominal values of the free-stream parameters in the working part of the SWT T-313 and their maximum deviations from experiment-to-experiment.

The degree of inhomogeneity of the Mach number fields M_∞ in the area where the model was located did not exceed 1% [5]. According to thermoanemometric measurements, the turbulence parameters in the oncoming external flow were characterized by the relative level of mass flow pulsations $\langle m \rangle / m = \langle \rho u \rangle / \rho u = 0.51\%$ and braking temperatures $\langle T_0 \rangle / T_{0\,c} = 0.03\%$. The relative level of velocity pulsations was $\langle u \rangle / u = 0.13\%$. In this case, the disturbances propagating in the flow were an acoustic mode of pulsations generated by the boundary layer on the walls of the nozzle and the working part of the SWT. The main measurements of pressure distributions on the surface of the model were carried out using a multichannel pneumatic commutator with class 0.2 strain gauges with a nominal value of 0.1 MPa. Class 0.5 group recording pressure gauges GPM-2 with measurement limits of 0–1 atm were also used. This guaranteed a measurement accuracy of not worse than 0.5%. Comparisons of the data obtained using these instruments showed good repeatability of the measurements, whose scatter was within 1%.

4. RECOMMENDED FORMULATION OF THE PROBLEM AND FORM OF PRESENTATION OF RESULTS

The formulation of the problem and the form of the presentation of the numerical results are partially described in [2]. Before starting the work, all the authors received files with a detailed assignment, as well as a mathematical model of the calculated geometry in the CAD format, initial data, draft recommended grids, tables with experimental results, and formats for presenting the results.

The calculated geometry completely reproduced the experimental model presented in Fig. 2. The exception was the vertical pylon, which was removed. The turbulator was modeled as a thin half-cylinder on the surface of the plate, as described in Section 3. For calculations with a natural laminar-turbulent transition (without taking into account the turbulator), a different geometry was provided with a plate twice as long. The flow parameters on the left boundary of the computational domain were set in accordance with the data in Table 2. The turbulence parameters were obtained by processing the experimental data and were equal to $Tu = 0.1\%$ ($Tu = u'/u_\infty \times 100$) and $\Omega = 200$ Hz. Depending on the features of the program code implementations, the authors could set turbulence parameters that differed from the recommended ones. The authors were allowed to use synthetic turbulence generator algorithms. To check the results obtained, the control section 1 is provided, located on the plate in front of the vacuum step. The experimental data in this section are given in Table 3 (index 1 corresponds to the outer boundary of the boundary layer). Achieving compliance gave hope that the laminar-turbulent transition was correctly taken into account in the calculation.

The dimensions of the computational domain are chosen in such a way that the reflected disturbances do not cross the studied area. In the outlet section, the block ends at the end of the model, which is correct in the case of supersonic flow outflow. There is a grid option with a buffer zone at the exit. Two versions of the block grid, structured and unstructured, were constructed. The presence of areas of high gradients in the contour break sections is taken into account. Near the surface of the step, the grid is refined according to the exponential law with the condition $y^+ = 1$ on the surface. It is recommended to use the following

Table 3. Flow parameters in control section 1

Model	M_1	p_0, kPa	P_1, kPa	T_1, K	δ, mm
BFS 45	2.9	381.6	12.06	292	5.08

boundary conditions: (1) adhesion to a thermally insulated wall on the surface; (2) supersonic inflow/outflow taking into account Riemann invariants at the outer boundaries (the outer boundaries of the computational domain are located at a sufficient distance from the separation zone); (3) the periodic condition on the lateral boundaries. The parameters of the undisturbed flow in all cells of the computational grid are set as the initial data.

When integrating over time, it is recommended to achieve convergence of the solution with an accuracy of at least 10^{-6} according to the total pressure at the worst point. If, for objective reasons, convergence does not occur, then it is recommended to start the averaging procedure after the solution reaches the limit cycle of oscillations. At least five cycles must be involved in averaging.

If computational capabilities are available, it is recommended to construct two more nested grids and check the convergence of the solution over the grids.

When processing the calculation results, the previously prepared tables should be used and the data should be filled strictly in the proposed order. Tabular material must be constructed in the form of graphs in the format [2].

5. TEST CALCULATION USING THE NOISEtte SOFTWARE OF KELDYSH IAM RAS

The NOISEtte calculation code [6] has been developed since the early 2000s. It implements an accurate vertex-centered finite-volume method that works on unstructured computational grids. The modern version of the NOISEtte code, which has high levels of parallel efficiency and scalability, allows large-scale calculations to be carried out on hybrid architecture supercomputers, optimally using CPU cores and graphics accelerators.

The NOISEtte eddy-resolving algorithm is built using a hybrid RANS-LES approach IDDES [7]. Turbulence (SA) [8] and SST [9] models were used as closure models. The calculations were performed using a hybrid adaptive numerical scheme [10], based on the original EBR approach [11] with increased accuracy and having a WENO extension [12] for flows with discontinuities. Integration over time was carried out using an implicit scheme of second order accuracy with linearization according to Newton. To solve a system of algebraic equations, the biconjugate gradient method was used. The time step was chosen from the condition that the local Courant number in the LES region (starting from a certain distance to the wall) did not exceed 1. Depending on the calculation, it was $1–2 \times 10^{-3} h/U_\infty$ (U_∞ is the external flow velocity). To create an unsteady turbulent flow upstream from the edge of the bench, a synthetic turbulence generator proposed in [13] was used, with the help of which the corresponding velocity pulsations were specified at the inlet boundary.

Figure 5 shows a fragment of an unstructured computational grid used to simulate the flow using the IDDES approach in the two-dimensional (XY) section. The input, output, and upper boundaries of the computational domain were respectively located at distances of 3 h, 50 h, and 50 h from the edge of the ledge. In the transverse direction, where periodicity conditions were imposed on the boundaries, the size of the computational domain was 1.5 h. The first near-wall grid step was chosen from the condition $y^+ \leq 1$, necessary for setting the adhesion conditions. In the longitudinal and transverse directions in the zone of the main turbulent interaction (from the inlet boundary $x/h = -3$ to $x/h = 8$ and from a hard surface to a distance ≈0.8 h), the grid steps did not exceed 0.017 h and 0.01 h, respectively. This was less than the $\delta_{0.99}/10$ for the step along the X coordinate and $\delta_{0.99}/20$ along the Z coordinate ($\delta_{0.99}$ was the boundary layer thickness), recommended for the IDDES calculation in the LES mode with near-wall modeling (WMLES mode). In the most sensitive area, in the area of the slope of the ledge, the grid was thickened so that $\Delta \leq 0.01h$ in the tangential direction. The run-up and thickening coefficients in the entire region did not exceed 1.1. The final size of the three-dimensional unstructured computational grid was 15.24 million nodes.

The computational domain for carrying out calculations within the NOISEtte code corresponded to the vortex-resolving calculation (flow direction, along the axis OX; normal to the wall, along the OY axis; and the transverse direction, along the OZ axis). At the input boundary ($x/h = -3$ from the edge of the

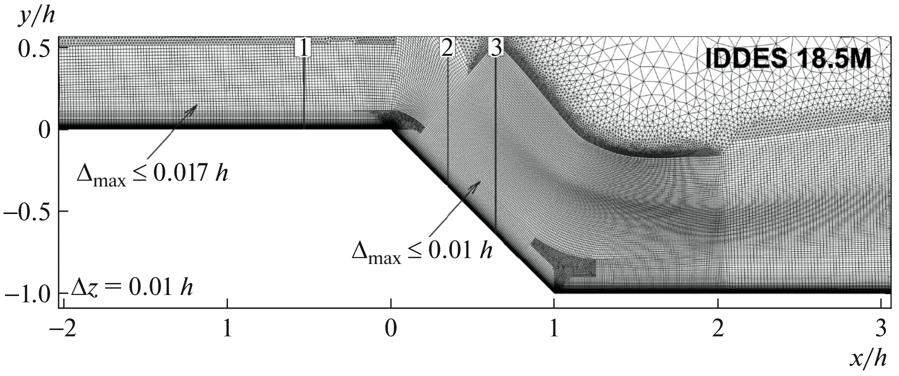

Fig. 5. Fragment of a computational grid for calculations using the IDDES model.

ledge), the profile for all variables obtained as a result of the preliminary calculation of the flat plate was kept. The values were chosen in such a way that the characteristics of the boundary layer (displacement thickness and momentum loss thickness) corresponded to the experimental value in the cross section $x/h = -0.53$. In addition, in the region $0 < y/h < 0.5$, nonstationary velocity pulsations were specified at the inlet boundary using a synthetic turbulence generator [13]. The output and upper boundaries were at a distance of 50 *h* from the edge of the ledge. The periodicity conditions were set in the transverse direction.

Using the NOISEtte code in the IDDES approach, two calculations were carried out on the A1 grid (see Table 4), differing in the turbulence model (SA and SST). The first calculation started with a 2D solution in the RANS approach (the second, with a nonstationary steady-state solution in SA IDDES). Further, starting from some time (from 10 to 30 h/U_∞), a statistically stationary mode was established and the process of data accumulation for averaging began. For all calculations, the sample length of the averaged characteristics was 50 h/U_∞. All the data in the 2D section, as well as the profiles along the model surface and diagrams of the total pressure behind a direct shock (Pitot pressure), were additionally spatially averaged along *OZ*.

All the calculations were carried out on graphics accelerators: a K60 hybrid cluster of Keldysh IAM RAS was used. Four NVIDIA Volta 100 GPUs were used. To obtain a sample of length 10 h/U_∞, on average about 2.1 h of physical time were required.

The physical features of the flow were studied in accordance with the test conditions. Figure 6 shows the flow pattern (averaged distribution of the density gradient modulus) for the SA NOISEtte turbulence model (the flow pattern is similar for the SST model). Visually, the flow picture is practically no different from the experiment. Both images highlight the main features such as the rarefaction wave fan, the main shock *2*, and the separation shock *1*.

The calculated picture of the separated flow is presented in Fig. 7. The streamlines are plotted against the background of the number field M. Markers mark the points at which the vertical velocity profile undergoes a break (points of zero velocity). The dotted lines are drawn through the markers, which separate the zones of direct and return flows in the separation. The points of intersection of the dotted lines with the surface of the step are the points of flow separation and attachment. They were determined experimentally using soot-oil spectra. A comparison of the calculated and experimental values of the *X* coordinate of flow separation and attachment are given in Table 5. It can be seen that the separation point is predicted an order of magnitude more accurately than the attachment point. The accuracy of determining the coordinates of separation and attachment is assessed by the following relations:

$$L_{\text{exp.}} = X_{R_{\text{exp.}}} - X_{S_{\text{exp.}}},$$

$$\delta_S\% = \left[\left|X_{S_{\text{calc.}}} - X_{S_{\text{exp.}}}\right|/L_{\text{exp.}}\right]\times 100\%, \quad \delta_R\% = \left[\left|X_{R_{\text{calc.}}} - X_{R_{\text{exp.}}}\right|/L_{\text{exp.}}\right]\times 100\%.$$

Table 4. Computational grids for calculations in the NOISEtte framework

Grid	N_{2D}	N_z	$N_{3D}/10^6$	L_z	$\Delta_{\max,\,\mathrm{BS}}$	Calculations
A1	97719	150	15.24	1.5 *h*	0.01 *h*	SST IDDES, SA IDDES

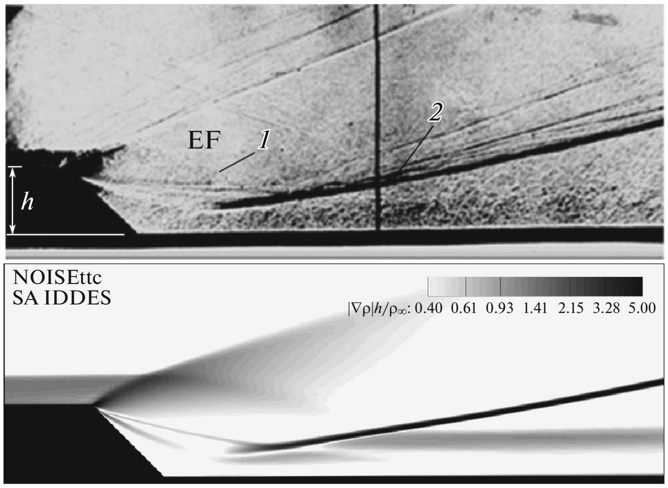

Fig. 6. Shadow photograph of the flow around an inclined ledge in experiment and calculation.

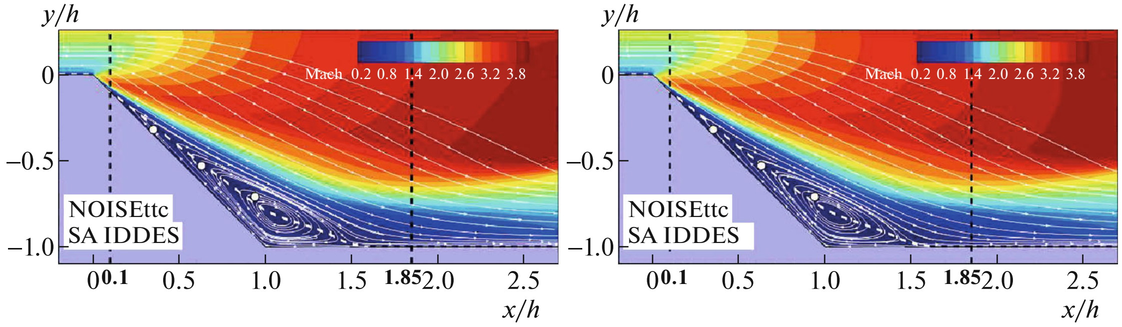

Fig. 7. Calculation of NOISEtte fields of Mach numbers and streamlines in the separation zone.

Table 6 presents the Y coordinates of the points located on the zero velocity line. The accuracy of determining the coordinates is estimated by the relation

$$\delta_Y\% = \left[\left|Y_{\text{calc.}} - Y_{\text{exp.}}\right| / Y_{\text{exp.}}\right] \times 100\%.$$

The characteristic dimensions of vortex structures such as Görtler vortices (see Fig. 4) are compared in Table 7. The accuracy of their determination is estimated using the formula

$$\delta_D\% = \left[\left|D_{\text{calc.}} - D_{\text{exp.}}\right| / D_{\text{exp.}}\right] \times 100\%.$$

Table 5. Calculation of NOISEtte points of flow separation and attachment (X coordinates)

	Exp.	Calc. SA	SA δ, %	Calc. SST	SST δ, %
Separation S	0.1 h	0.097 h	$\delta_S\% = 0.1$	0.0985 h	$\delta_S\% = 0.1$
Attachment R	1.85 h	1.63 h	$\delta_R\% = 12.5$	1.67 h	$\delta_R\% = 10$

Table 6. Calculation of NOISEtte points of the zero velocity line (X and Y coordinates)

X	Exp. (Y)	Calc. SA	SA δ_Y, % (Y)	Calc. SST	SST δ_Y, % (Y)
0.35 h	–0.32 h	–0.297 h	7	–0.297 h	7
0.63 h	–0.53 h	–0.516 h	2.6	–0.521 h	1.7
0.94 h	–0.71 h	–0.75 h	5.6	–0.746 h	5

Table 7. NOISEtte calculation of characteristic sizes of vortex structures

	Exp.	Calc. SA	SA δ_D, %	Calc. SST	SST δ_D, %
Size of vortex structures	0.53 *h*	0.5 *h*	5.6	0.52 *h*	2

They were obtained based on measurements of the limiting current lines (see Fig. 8), which are depicted using the averaged distributions of the friction stress vector on the walls.

A graph of the distribution of relative values of static pressure over the surface of the tandem step model in the symmetry plane is shown in Fig. 9. The pressure before the break of the step contour in Section 1 ($x/h = -0.53$) was chosen as the characteristic value. The standard deviation (SD) $\Delta = \sqrt{\Sigma(x_i - x_{i\,\mathrm{exp}})^2/N}$ of the calculated and experimental pressure values are, respectively, $\Delta_{\mathrm{SA}} = 0.0229$ for the IDDES SA method and $\Delta_{\mathrm{SST}} = 0.0219$ for the IDDES SST method. The maximum differences between the calculated and experimental data are observed in the vicinity of the nose of the compression step ($x/h = 1$).

The diagrams of the relative Pitot pressure values are shown in four sections (Fig. 10). The Pitot pressure at the outer boundary of the boundary layer in section 1 was chosen as the characteristic value. The graphs are plotted along the Y axis in sections: x/h = (1) –0.53, (2) 0.35, (3) 0.64, (4) 5.22.

The SD of the calculated experimental values of the Pitot pressure are given in Table 8. The maximum differences between the calculated and experimental data are observed in the diagrams constructed in sections 1 and 4.

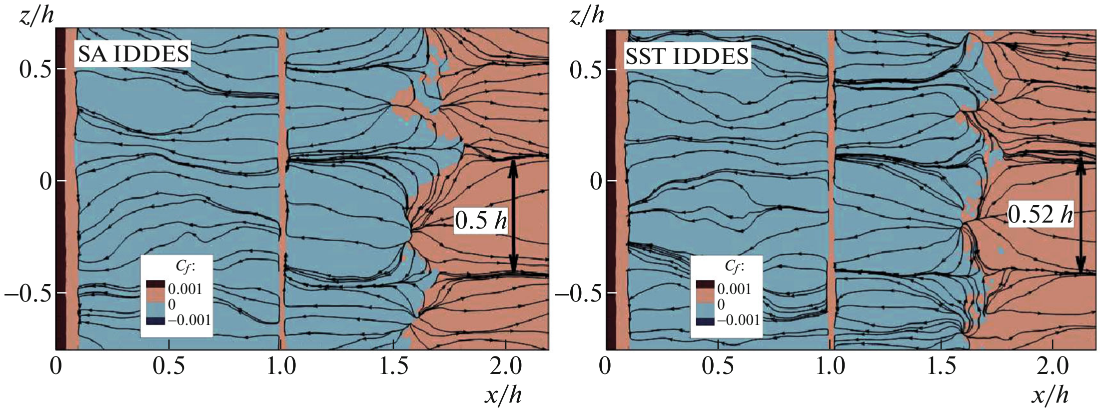

Fig. 8. Calculation of NOISEtte limit streamlines on the surface of tandem steps.

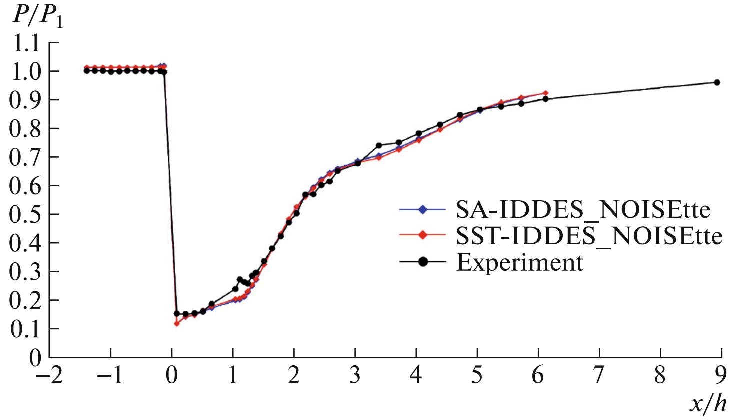

Fig. 9. NOISEtte calculation of static pressure on the surface of tandem steps.

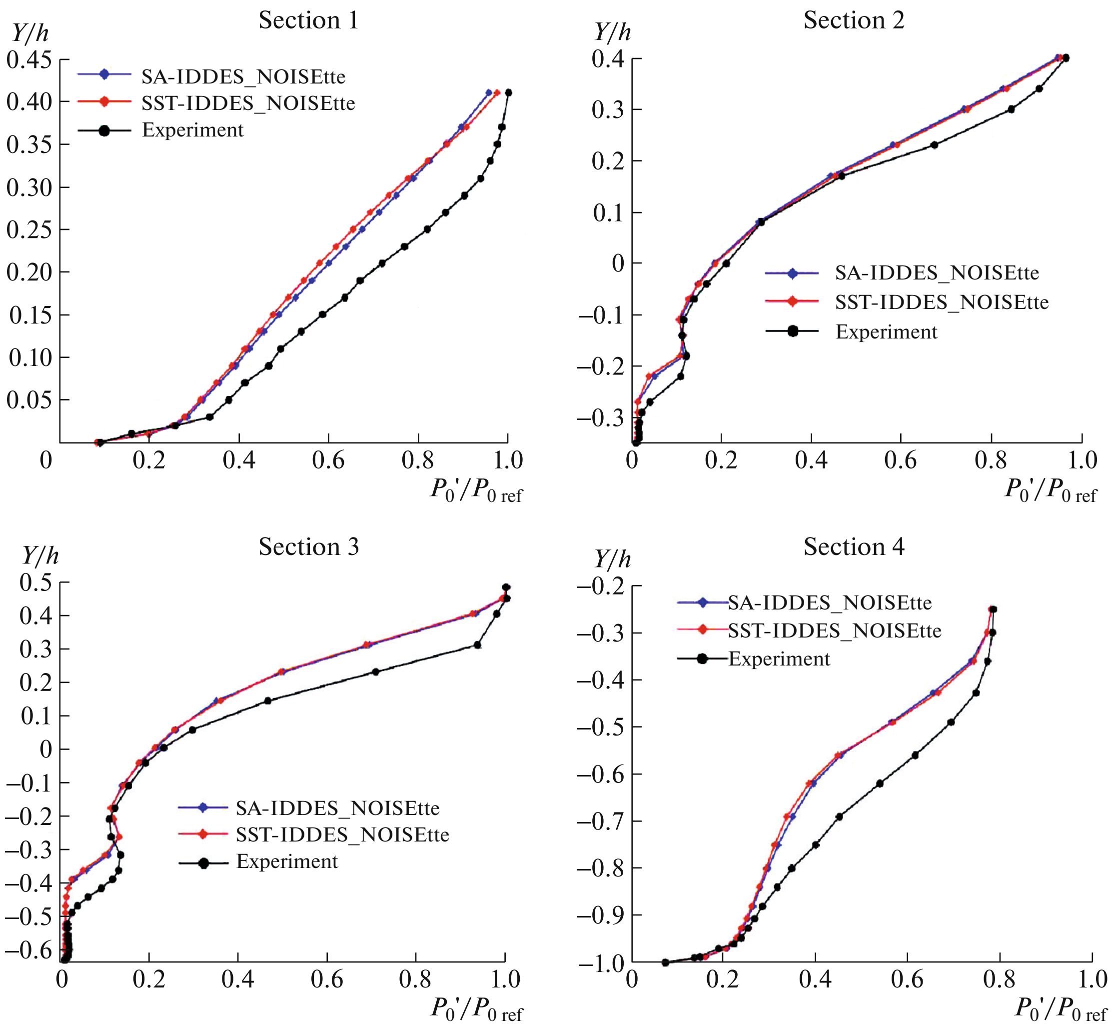

Fig. 10. NOISEtte calculation of Pitot pressure diagrams in given sections.

6. TEST CALCULATION USING THE RUSSIAN FEDERAL NUCLEAR CENTER—ALL-RUSSIAN RESEARCH INSTITUTE OF EXPERIMENTAL PHYSICS LOGOS SOFTWARE

The LOGOS software package has been developed since 2010 and is intended for modeling processes of heat and mass transfer, the stress-strain state, and the flow of multiphase media, as well as solving multiphysics problems. The main purpose of the product is to solve a wide range of industrial problems. The Logos Aero-Hydro module is designed to simulate heat and mass transfer problems [14–17]. The module includes a complete set of tools for carrying out the entire chain of the solution of a problem, from working with a geometric model to analyzing the calculation results. The module uses the finite volume method to solve the Navier–Stokes equations. The cells of the computational domain generally represent arbitrary

Table 8. SD from experiment for Pitot pressure values in NOISEtte calculation

X	ΔSA	ΔSST
$-5.22\,h$	0.1005	0.1108
$0.35\,h$	0.0405	0.0384
$0.64\,h$	0.0674	0.0693
$5.22\,h$	0.0692	0.0716

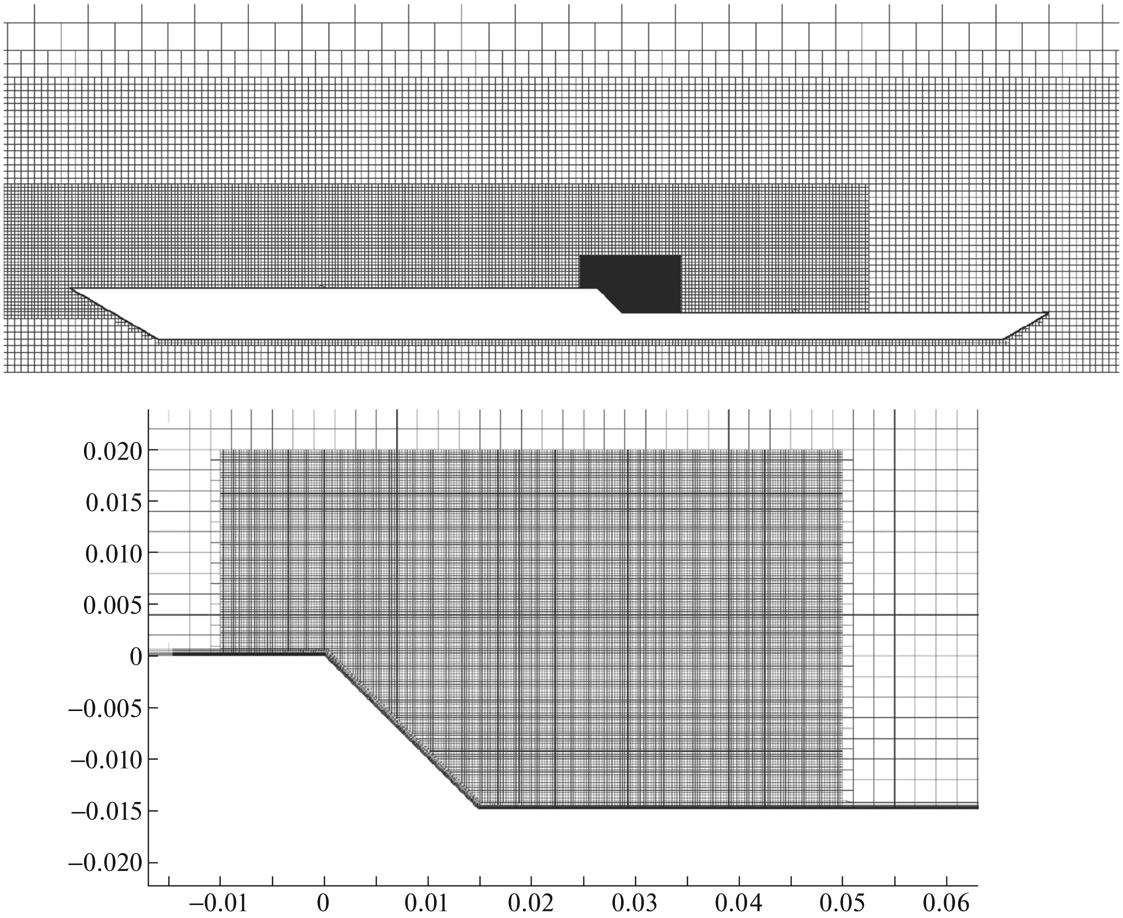

Fig. 11. Fragment of the computational grid in the central section.

polyhedra. To solve problems of external aerodynamics, as a rule, grids of cut-off hexagons with the selection of prismatic layers are used.

RANS modeling of the problem was carried out using the system of Reynolds-averaged Navier–Stokes equations. The values of the molecular component of the tangential stress tensor of a Newtonian medium satisfy Newton's rheological law, which provides connections between the viscous stress tensor and the strain rate tensor, and the components of the heat flux density vector are related to the local temperature gradient by Fourier's law. The dynamic viscosity coefficient $\mu(T)$ and thermal conductivity coefficient $\lambda(T)$, depending on the flow temperature, are determined by the Sutherland formula.

This test uses the SA-R turbulence model [18]. To approximate convective flows, the AUSMPW scheme with second-order spatial discretization accuracy is used.

To solve the problem, we used a computational grid constructed in LOGOS [19] based on truncated hexahedrons with prismatic layers (Fig. 11). A local grinding zone was introduced in the ledge area. The computational grid has the following characteristics: there are a total of approximately 36 million cells, the characteristic linear size of a cell in the direction *OX* and *OY* in the local subarea is 0.16 h (25 mm), the characteristic linear cell size in the direction *OZ* in the local subarea is 0.32 h (50 mm), the thickness of the first cell of the boundary layer is 6.7e^{-5} h (0.001 mm), the prismatic layer thickness is 5h (75 mm), and there are 20 prismatic layers.

The initial conditions were set to a homogeneous viscous gas flow with the following parameters: $P_\infty = 11\,200$ Pa, $T_\infty = 103.84$ K, $M_\infty = 3.01$, the Reynolds number reduced to the characteristic size $h = 0.015$ m, and $\mathrm{Re} = 1.347 \times 10^7$.

In the flow around a tandem of steps, a picture was obtained that qualitatively coincided with the experimental one. A fan of rarefaction waves propagates from the top of the ledge into the external flow (see Fig. 12 and experiment in Fig. 6). As a result of the separation of the boundary layer below the top

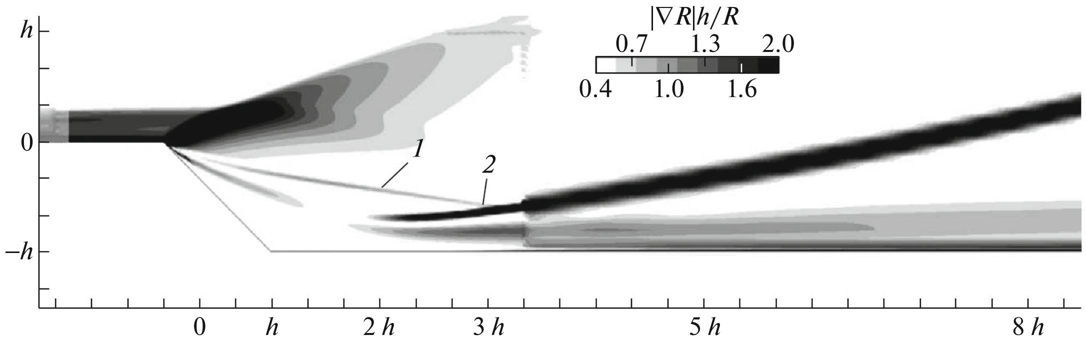

Fig. 12. LOGOS calculation of the flow pattern around a tandem step (density gradients).

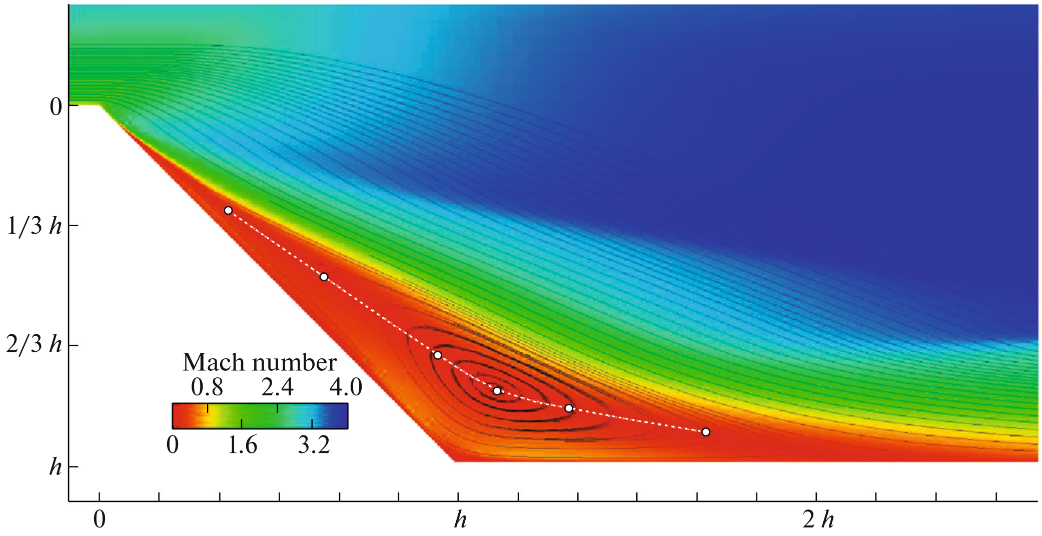

Fig. 13. LOGOS calculation of Mach number fields and streamlines in the separation zone.

from the surface of the inclined face, a separation shock wave (*1*) is formed, and when the flow turns parallel to the surface behind the step, the main shock (*2*) is formed, which is actually the initiator of the separation.

Figure 13 shows the Mach number fields and streamlines obtained in the calculations, which characterize the return flow in the separation zone behind the step in the vertical section coinciding with the plane of symmetry of the model.

The dashed line indicates the experimentally recorded position of the line of zero longitudinal velocity, which separates the zones of forward and return flows. Table 9 shows the coordinates of the lines (points) of separation (S) and attachment (R), which were obtained experimentally and by calculation (indicated in Fig. 1), and in Table 10 the coordinates of points on the line of zero velocities are compared.

Figure 14 shows the calculation results and estimates of the characteristic parameters of the vortex structures. A comparison with the experiment shows that the calculated size of the vortex structures such as Görtler vortices is slightly larger than the corresponding size obtained in the experiment (see Table 11).

Table 9. LOGOS calculation of flow separation and attachment points (X coordinate)

	Exp.	Calc. SA-R	δ, %
Separation S	$0.1\,h$	$0.08\,h$	$\delta_S\% = 1$
Attachment R	$1.85h$	$2.3\,h$	$\delta_R\% = 25$

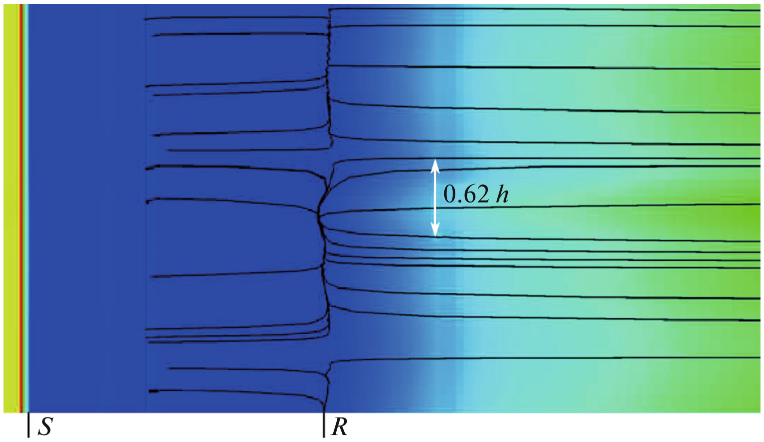

Fig. 14. LOGOS calculation of limiting streamlines on the surface of tandem steps.

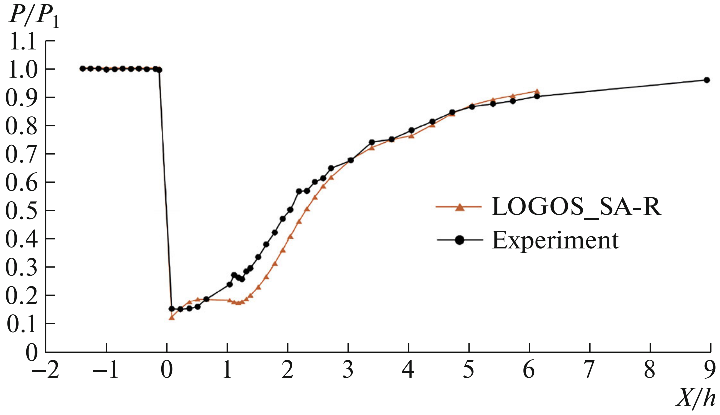

Fig. 15. LOGOS calculation of static pressure on the surface of tandem steps.

A graph of the distribution of the relative values of static pressure over the surface of the tandem step model is shown in Fig. 15.

The SD of the calculated and experimental pressure values when using the SA-R turbulence model is estimated by the value $\Delta = 0.0546$. The maximum differences between the calculated and experimental data are observed in the vicinity of the horizontal section of the model after the compression step ($x/h = 1–3$).

Table 10. Calculation of LOGOS points on the line of zero velocities (Y coordinates)

X	Exp. (Y)	Calc. SA-R (Y)	δ_Y, % (Y)
0.35 h	–0.32 h	–0.288 h	2
0.63 h	–0.53 h	–0.475 h	3
0.94 h	–0.71 h	–0.708 h	0.1

Table 11. LOGOS calculation of characteristic sizes of vortex structures

	Experiment	SA-R calculation	δ_D, %
Size of vortex structures	0.53 h	0.62 h	17

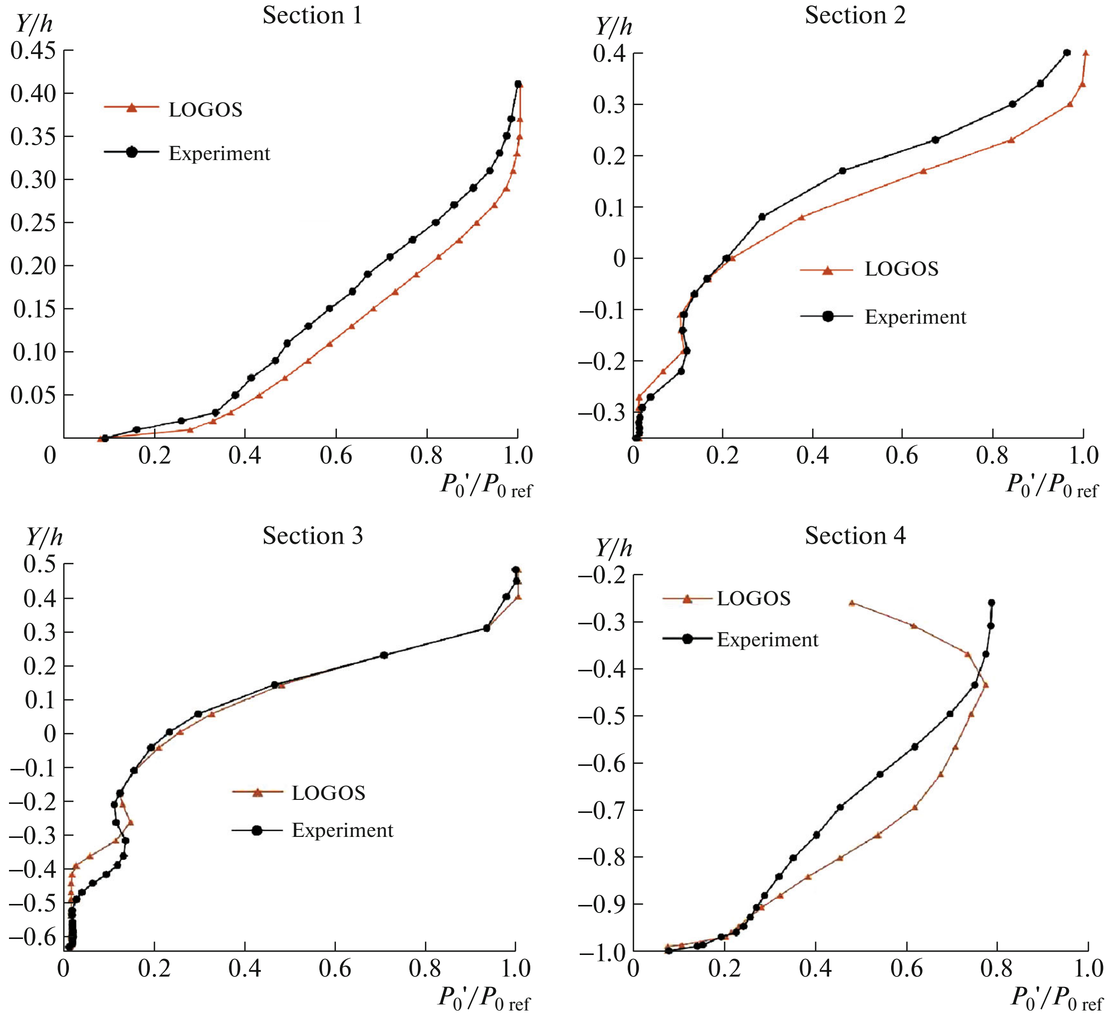

Fig. 16. LOGOS calculation of Pitot pressure diagrams in given sections.

Diagrams of the relative Pitot pressure values plotted along the *Y* coordinate are shown in four sections; see Fig. 16.

The SD of the calculated and experimental Pitot pressure values are given in Table 12.

Table 12. SD from experiment for Pitot pressure values in LOGOS calculation

X	−5.22 *h*	0.35 *h*	0.64 *h*	5.22 *h*
Δ SA-R	0.0783	0.0697	0.0295	0.1051

The maximum differences between the calculated and experimental data are observed in the diagrams constructed in sections 1, 2, and 4.

7. TEST CALCULATION USING THE ZHUKOVSKY TsAGI GRAT SOFTWARE

This section presents the results obtained using the GRAT computer code [20–22]. The code is based on a numerical solution by the finite volume method of the system of Navier–Stokes equations, closed by a modified two-parameter SST-2003 turbulence model [9]. The first difference from the original model was the use of the vorticity tensor (rather than the strain rate tensor) in writing the turbulence production term. The second difference was taking into account the compressibility of the gas. In addition, to stabilize

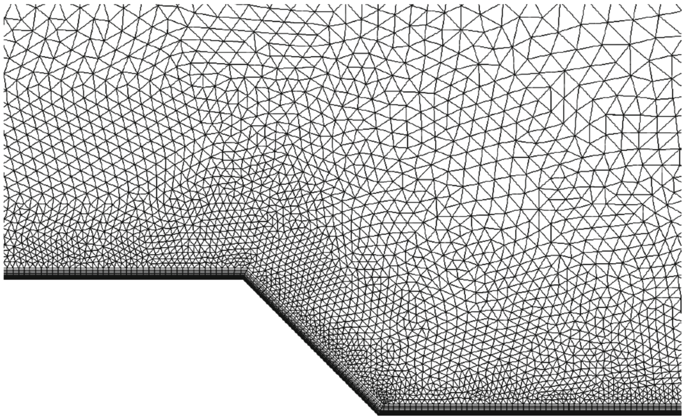

Fig. 17. Fragment of the computational grid.

the solution, a restriction was introduced on the minimum value of density and, as a consequence, pressure. In some cases (for example, in the return flow zones), this could lead to the emergence of a nonphysical solution.

The problem was solved using the modified AUSM method of splitting convective flows, which has proven itself in numerous calculations. To increase the order of accuracy of the numerical solution in space to the second order, a linear reconstruction procedure was carried out. For integration over time, an explicit method of first order accuracy was used. In this case, integration was carried out until a stationary state was achieved.

The calculations use an unstructured grid, an important advantage of which is the automation of the construction of any geometric configurations. Figure 17 shows a fragment of such a grid in the plane of symmetry of the model. The tetrahedral and prismatic elements are used as finite volumes. The height of the first cell, related to the height of the ledge, was 0.0001 h. The number of cells in the three-dimensional implementation of the grid was 10.3 million elements.

On the surface of a streamlined body with a thermally insulated wall, no-slip boundary conditions were specified. The described algorithm is implemented using parallel computing technologies based on the OpenMP and MPI platforms. This made it possible to efficiently distribute computer resources and obtain a solution in an acceptable time period.

Based on the calculation results, visualization was performed by plotting in Fig. 18 the distribution of the density gradients, which is an analog of the shadow photographs obtained in the experiment.

All the main elements that determine the physics of the flow are present in Fig. 18. In the area of the outer ledge, there is a fan of rarefaction waves. The separation of the boundary layer is easily distinguished, which is initiated by the main shock wave *2*, followed by the separation shock wave *1*. Figure 19 shows the calculated fields of Mach numbers and streamlines that characterize the return flow in the separation zone behind the step.

Table 13 shows a comparison of the coordinates of the points of separation (S) and attachment (R), which were obtained experimentally and by calculation.

Table 14 shows a comparison of values of the Y coordinate points located on the line of zero velocities with the experimental data.

Figure 20 shows a picture of the limiting streamlines on the surface of the step. The boundaries of vortex structures such as Görtler vortices are clearly visible. A comparison of the calculated and experimental values for the vortex diameters is given in Table 15.

Table 13. Calculation of GRAT points of flow separation and attachment (X coordinate)

	Exp.	Calc. SST	δ, %
Separation S	0.1 h	0.14 h	$\delta_S\% = 2$
Attachment R	1.85 h	1.95 h	$\delta_R\% = 6$

Table 14. Calculation of GRAT points on the line of zero velocities (Y coordinates)

X	Exp. (Y)	Calc. SST (Y)	δ_Y, %
0.35	−0.32	−0.31	3
0.63	−0.53	−0.51	3.7
0.94	−0.71	−0.73	2.8

Table 15. Calculation of GRAT characteristic sizes of vortex structures

	Exp.	Calc. SST	δ_D, %
Size of vortex structures	0.53 h	0.73 h	38

Table 16. SD from the experiment for Pitot pressure values in the GRAT calculation

X	−5.22 h	0.35 h	0.64 h	5.22 h
Δ SST	0.0387	0.0507	0.0296	0.0524

A graph of the distribution of the relative values of static pressure over the surface of the tandem step model is shown in Fig. 21. The relative pressure in section 1 is $p/p_1 = 1$. The SD of the calculated and experimental pressure values when using the SST turbulence model is estimated by the value $\Delta = 0.126$. The maximum differences between the calculated and experimental data are observed at the surface of the rarefaction step ($x/h = 0$–1).

Diagrams of relative Pitot pressure values plotted along the Y coordinate are shown in four sections; see Fig. 22.

The SD of the calculated and experimental Pitot pressure values is given in Table 16.

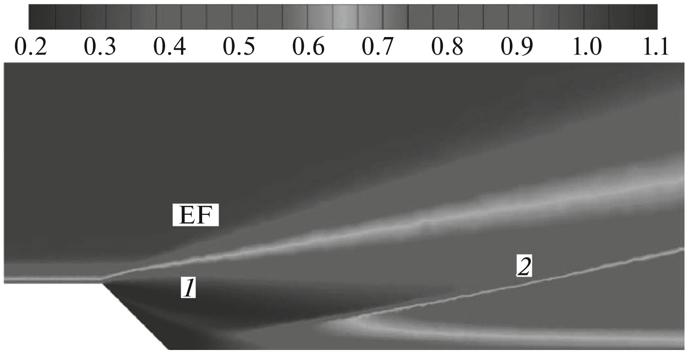

Fig. 18. Calculation of the GRAT pattern of flow around a tandem step (density gradients).

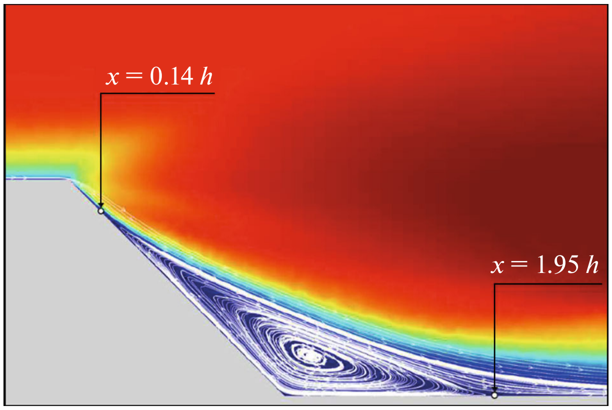

Fig. 19. Calculation of GRAT fields of Mach numbers and streamlines in the separation zone.

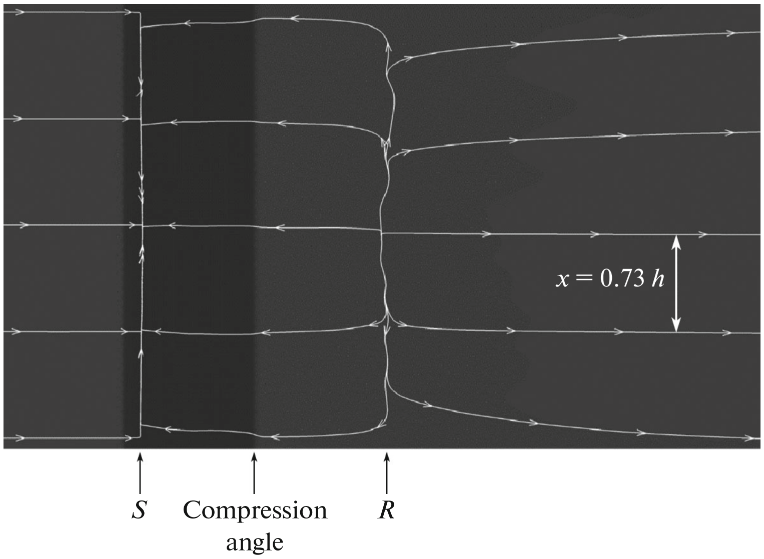

Fig. 20. Calculation of GRAT limit streamlines on the surface of tandem steps.

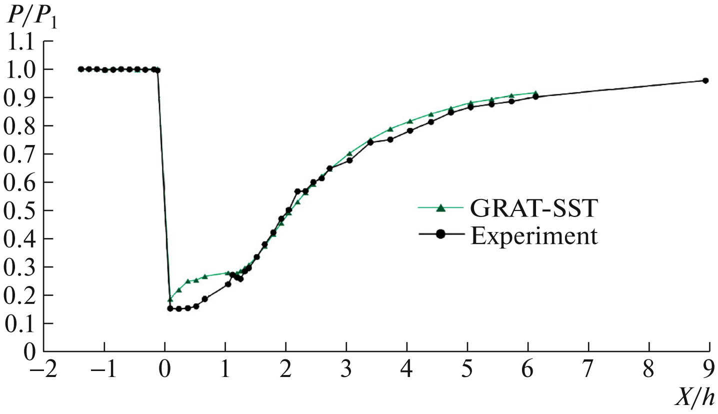

Fig. 21. Calculation of static pressure GRAT on the surface of tandem steps.

The maximum differences between the calculated and experimental data are due to the horizontal shift of the diagrams in sections 2 and 4.

8. TEST CALCULATION USING IRKUT CORPORATION'S ANSYS FLUENT SOFTWARE

This section presents the results obtained using the ANSYS Fluent computer code [23]. The studies were carried out within the framework of the system of Reynolds-averaged Navier–Stokes equations. To solve the basic gasdynamic equations, the density base solver was chosen, because according to the user's guide [23], it clearly describes flows with compressibility effects and shock waves. To close the system of Reynolds equations, the Spalart–Allmaras SA model [8] and the k–ω SST model [9] were used. Together with this, corrections for the curvature of streamlines were taken into account for the SA-RC turbulence models [24] and k–ω SST-RC [25]. The derivatives were approximated by first-order schemes at the start of the solution and then switched to the second order.

To solve the problem, a structured block hexahedral computational grid consisting of 5627160 cells was used; see Fig. 17. There are 50 nodes along the step width; and 70, along the step length. The size of the near-wall cell in the zone of the compression stage is 0.0003 mm. The specified condensation of grid lines to the surfaces ensured the fulfillment of the condition $y^+ = 1$. In a special way, the grid was also con-

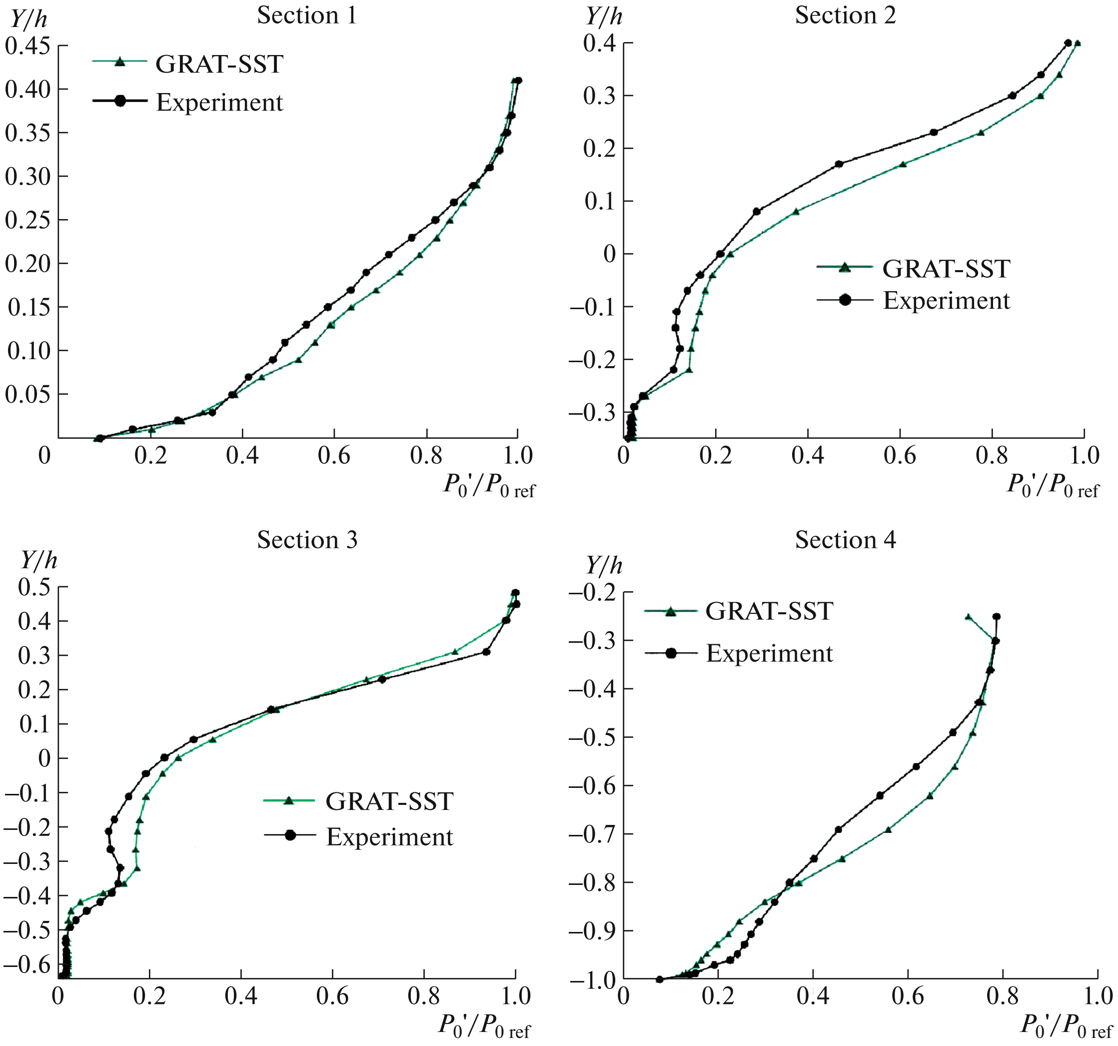

Fig. 22. Calculation of GRAT diagrams of Pitot pressure in given sections.

densed in places where the contour of the tandem steps was broken for a better description of the rarefaction wave and shock wave. The wire turbulator on the nose of the plate is clearly marked with a grid; see Fig. 23.

At the front, the upper and lower boundaries of the computational domain and the pressure far-field boundary conditions were set in terms of Fluent [23] with the following parameters: the Mach number $M = 3.01$, pressure $P = 11\,200$ Pa, and temperature $T = 103.84$ K. The periodic boundary conditions were established at the lateral boundaries of the computational domain. At the back boundary (technically these are two zones separated by the lower and upper surfaces of the step), the pressure outlet boundary conditions were set with the values $P = 11\,200$ Pa and $T = 103.84$ K.

Based on the calculation results, visualization was performed by plotting in Fig. 6 the distribution of the density gradients, which is an analog of the shadow photographs obtained in the experiment. As an example, the article presents a solution obtained using the SA-RC turbulence model, since the SST-RC model gives an almost identical picture. For clarity, the flow diagram is supplemented with limit lines; see Fig. 24. The indicated diagram contains a fan of rarefaction waves, two shock waves (SWs), the points of the flow's separation *S*, and attachment *R*, respectively. Table 17 shows a comparison of the calculated and experimental values of coordinate *X* of flow separation and attachment points for all tested turbulence models. An analysis of the error values shows that in this case, specialized turbulence models taking into

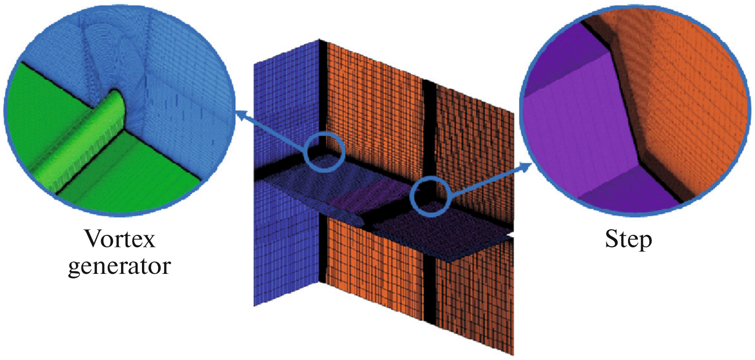

Fig. 23. Calculation grid for ANSYS Fluent.

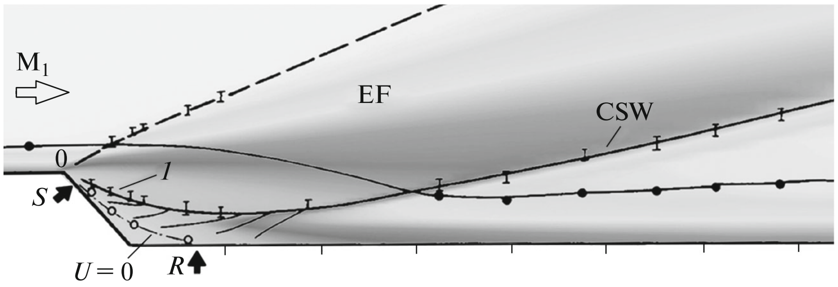

Fig. 24. Calculation of Fluent flow pattern around tandem steps (density gradients).

account the curvature of the SA-R and SST-R streamlines do not make it possible to fundamentally improve the prediction of the position of the points of the flow's separation *S* and attachment *R* compared to the original versions of the SA and SST models.

Figure 25 shows the Mach number fields and flow lines obtained in calculations using the SA turbulence model. The flow zone behind the step is presented in the vertical section coinciding with the plane of symmetry of the model. The number of fields M, obtained using the turbulence models SST, SA-R, and SST-R, are qualitatively similar to what is presented in Fig. 25, and are not presented in this article in order to shorten the text.

Table 18 shows a comparison of the calculated and experimental values of the coordinates of points located on the line of zero velocities located inside the separation zone.

The following are the limiting streamlines on the step surface calculated using the SA-RC turbulence model; see Fig. 26.

It should be noted that the secondary currents, i.e., Görtler vortices, were obtained only using the SA-RC and SST-RC turbulence models. The flow pattern obtained using the SST-RC model is qualitatively identical to the pattern presented in Fig. 20. The vortex structures are regular, and the limit lines are

Table 17. Calculation of Fluent flow separation and attachment points (*X* coordinate)

	Exp.	Calc. SA	SA δ, %	Calc. SST	SST δ, %
Separation *S*	0.1 *h*	0.06 *h*	$\delta_S\% = 2$	0.04 *h*	$\delta_S\% = 3.5$
Attachment *R*	1.85 *h*	2.67 *h*	$\delta_R\% = 47$	3.16 *h*	$\delta_R\% = 75$
	Exp.	SA-RC	SA-RC δ, %	SST-RC	SST δ, %
Separation *S*	0.1 *h*	0.08 *h*	$\delta_S\% = 1$	0.04 *h*	$\delta_S\% = 3.5$
Attachment *R*	1.85 *h*	2.55 *h*	$\delta_R\% = 40$	3.04 *h*	$\delta_R\% = 68$

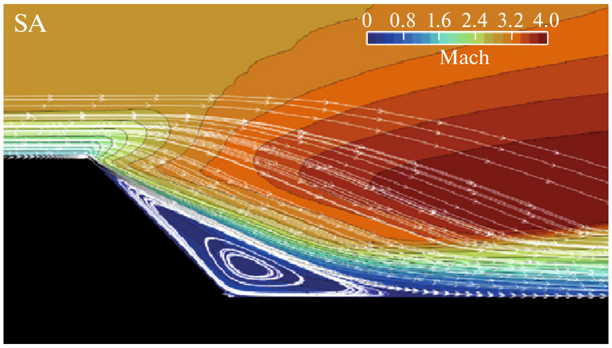

Fig. 25. Calculation of Fluent fields of Mach numbers and streamlines in the separation zone.

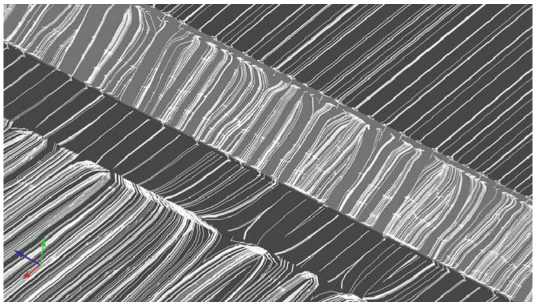

Fig. 26. Calculation of Fluent limit streamlines on the surface of tandem steps.

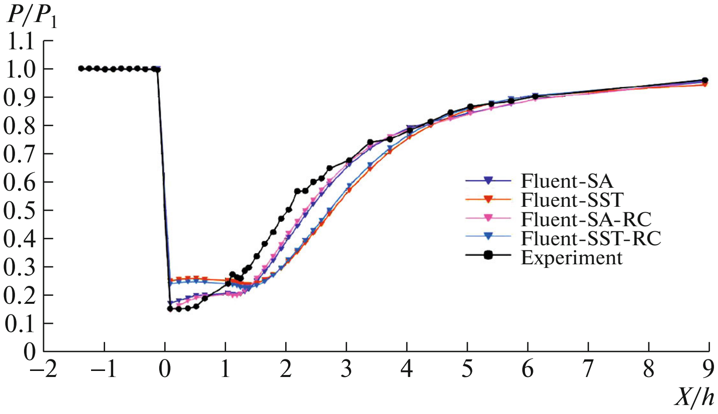

Fig. 27. Calculation of Fluent static pressure on the surface of tandem steps.

almost parallel. Table 19 compares the calculated and experimental values of the diameters of the vortex structures and estimates the accuracy of the calculated data.

A graph of the distribution of the relative values of static pressure over the surface of the tandem step model is shown in Fig. 27. The basic SA and SST models, as well as their modifications SA-R and SST-R, are presented.

The SD of the calculated and experimental pressure values obtained using various turbulence models is presented in Table 20.

A significant difference between the calculated and experimental data is observed along the entire length of the tandem steps. At the rarefaction stage, the calculated pressure levels are overestimated compared to the experimental ones (x/h = 0.02–1.0), and at the compression stage they are underestimated

Table 18. Calculation of Fluent points of the line of zero velocities (X and Y coordinates)

X	Exp. (Y)	Calc. SA	SA δ_Y, % (Y)	Calc. SST	SST δ_Y, % (Y)
0.35 h	−0.32 h	−0.27 h	15.6	−0.22 h	31
0.63 h	−0.53 h	−0.46 h	13	−0.37 h	30
0.94 h	−0.71 h	−0.69 h	2.8	−0.62 h	12.7
X	Exp. (Y)	SA-RC	δ_Y, % (Y)	SST-RC	δ_Y, % (Y)
0.35 h	−0.32 h	−0.28 h	12.5	−0.22 h	31
0.63 h	−0.53 h	−0.48 h	9	−0.37 h	30
0.94 h	−0.71 h	−0.71 h	0	−0.62 h	12.7

Table 19. Calculation of Fluent characteristic sizes of vortex structures

	Exp.	Calc. SA-RC	δ_D, %	Calc. SST-RC	δ_D, %
Size of vortex structures	0.53 h	1.67 h	215	1.36 h	157

Table 20. SD values of static pressure in the Fluent calculation

Turbulence model	S.A.	SST	SA-R	SST-R
Δ	0.0530	0.0920	0.0460	0.0880

Table 21. SD from the experiment for Pitot pressure values in the Fluent calculation

X	ΔSA	ΔSST	ΔSA-R	ΔSST-R
−5.22 h	0.0281	0.0328	0.0258	0.0312
0.35 h	0.0234	0.0385	0.0211	0.0376
0.64 h	0.0281	0.0328	0.0258	0.0312
5.22 h	0.0530	0.1079	0.0455	0.1043

($x/h > 1$). Modification of the basic turbulence models does not lead to a noticeable improvement in the result.

Diagrams of the relative Pitot pressure values plotted along the Y coordinate, are shown in four sections; see Fig. 28.

The SD of the calculated and experimental Pitot pressure values is given in Table 21.

The maximum difference between the calculated and experimental data is due to calculation errors in the return flow zone and is manifested in the diagrams in sections 2, 3, and 4.

9. TEST CALCULATION USING IRKUT CORPORATION'S FlowVision SOFTWARE

The FlowVision software package [26] is designed for the numerical modeling of three-dimensional laminar and turbulent, stationary and unsteady liquid and gas flows. The software package is based on the finite volume method, high-precision difference schemes, effective numerical methods, and reliable mathematical models of physical processes. Numerous models make it possible to simulate complex flows accompanied by the swirling of the flow, movement of contact surfaces, shock waves, coupled heat transfer, combustion, etc.

The FlowVision computational grid is Cartesian and locally adaptive. Local dynamic adaptation of the initial grid is performed in accordance with user-specified criteria. The initial grid consists of rectangular cells. Near the boundary of the computational domain, the Boolean subtraction of the noncalculated volumes from rectangular cells occurs, as a result of which polyhedron cells of arbitrary shape are formed. Grid generation is fully automated.

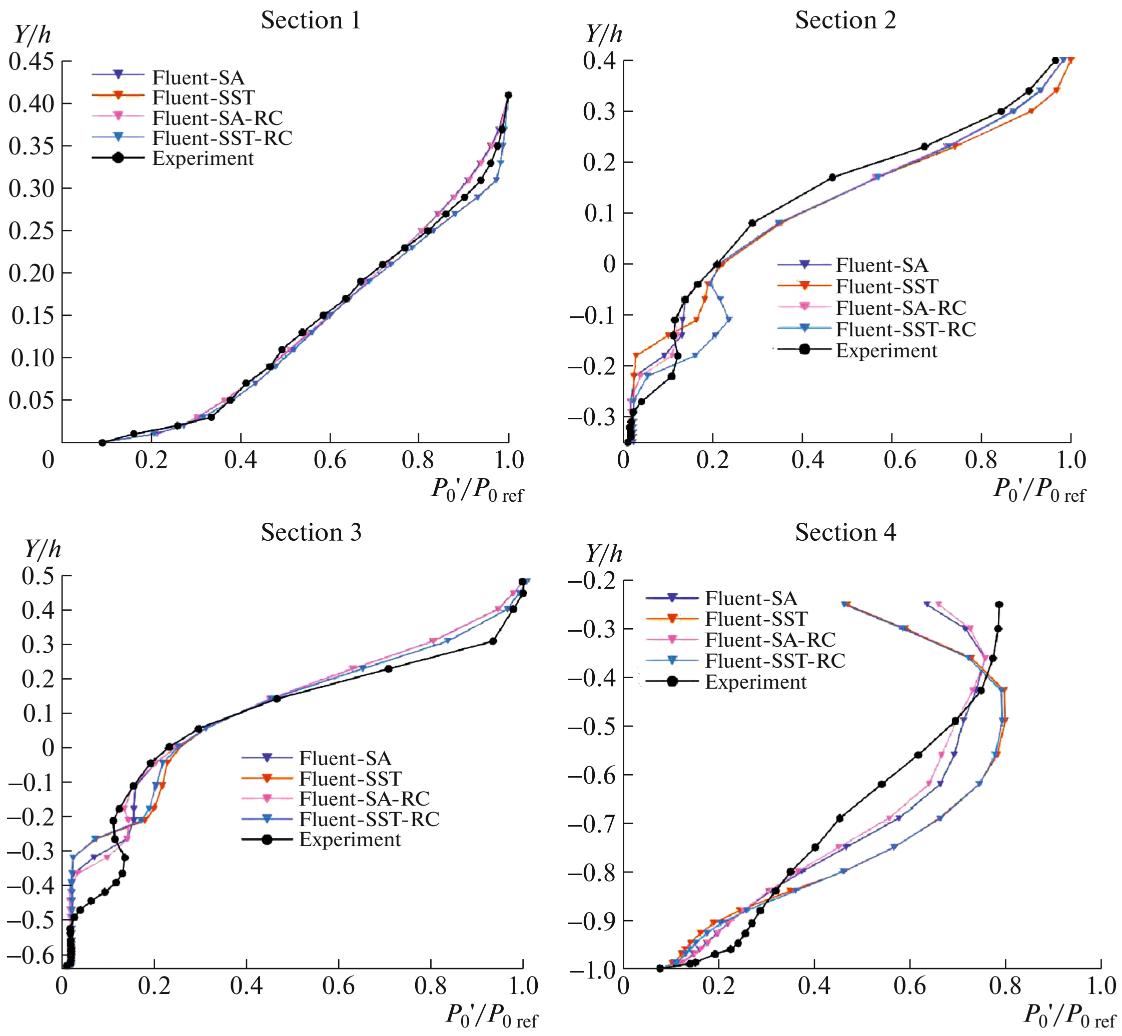

Fig. 28. Calculation of Fluent Pitot pressure diagrams in given sections.

The FlowVision software package runs on computers with a mixed architecture and combines internodal MPI parallelization with MP parallelization. Using mixed parallelization allows us to achieve high-quality scaling when working on a large number of processors.

The calculation was performed in the system of Reynolds-averaged Navier–Stokes equations, and closed by the Spalart–Allmaras SA model [8]. The periodic boundary conditions were established at the lateral boundaries of the computational domain. At the upper, lower, and rear boundaries of the computational domain (technically, the rear boundary consists of two zones separated by the lower and upper surface of the step), the free exit boundary conditions with pressure values $P = 11\,256$ Pa and temperature $T = 103.84$ K were set. At the front boundary, the input/output boundary conditions were set in terms of the FlowVision software [26] with the following parameters: Mach number M = 3.01, pressure $P = 11\,256$ Pa, and temperature $T = 103.84$ K.

To solve the problem, an orthogonal structured locally adaptive grid was constructed; see Fig. 29. The maximum level of grid adaptation is 2 (in terms of [27]), and the number of layers of each level is 6. The near-surface grids function was not used. There are 6294894 cells in the grid. The main dimensions of the computational grid are specified by the following parameters: the number of cells along the step width is 212 (at the lower level of adaptation), the number of cells along the step length is 872, the number of cells along the step height is 120, the size of the near-wall cell in the compression step zone is 0.25 mm. The grid is condensed in the area of the leading edge of the model, the area of the ledge, and on all surfaces.

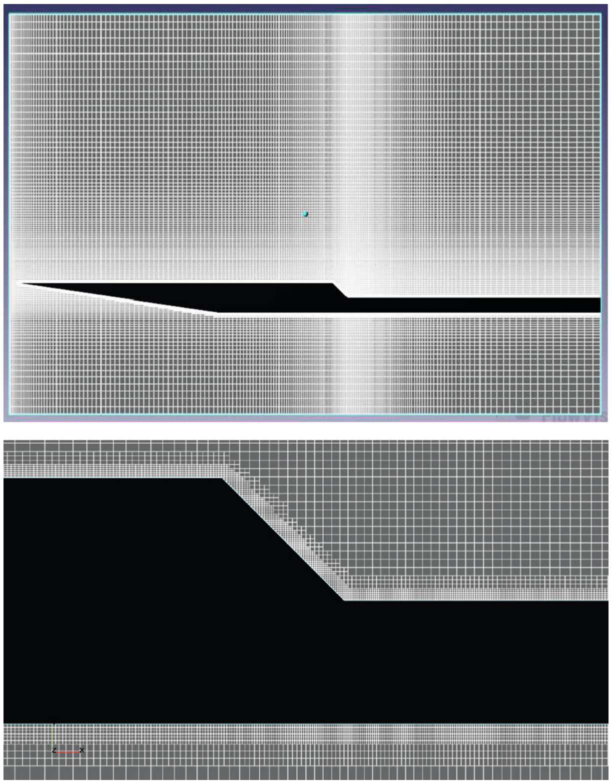

Fig. 29. Calculation grid for FlowVision (fragment).

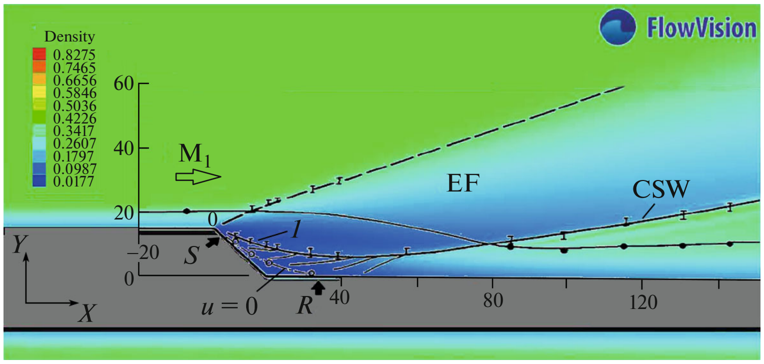

Fig. 30. FlowVision calculation of the flow pattern around a tandem step.

Based on the calculation results, the density function was visualized, allowing a comparison of the calculation with the experiment (see Fig. 6). For clarity, the flow diagram is supplemented with limit lines; see Fig. 30.

In Fig. 30 we can distinguish a fan of rarefaction waves, shock waves, and points of separation *S* and attachment *R* of the flow. Table 22 shows the calculated and experimental values of the *X* coordinate for points *S* and *R*. The data from the table are correlated to the Fluent results obtained for the SA turbulence model; see Table 17.

Figure 31 shows the Mach number fields and flow lines that visualize the return flow zone. The figure clearly shows the flow's separation point.

The graph of zero velocity lines for the experiment and calculation is shown in Fig. 32. It clearly demonstrates the fact of the late attachment of the separation. Table 23 contains the relative coordinates of the zero velocity lines for the experiment and numerical calculation.

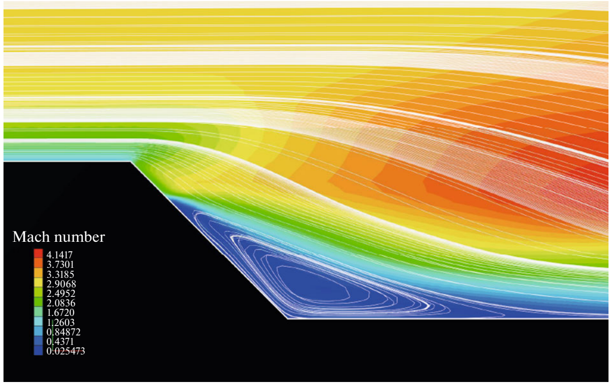

Fig. 31. FlowVision calculation of Mach number fields and streamlines in the separation zone.

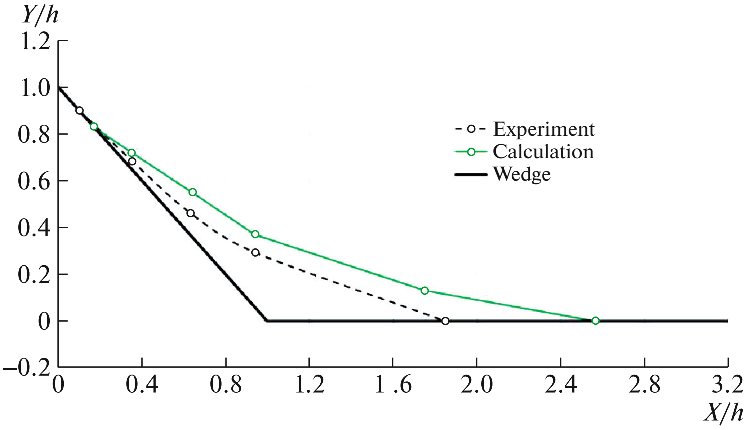

Fig. 32. FlowVision calculation of the zero velocity line in the separation zone.

Next, the limiting streamlines on the surface of the tandem steps are presented and an estimate of the diameter of vortex structures such as Görtler vortices is given; see Fig. 33. Table 24 compares the calculated and experimental values of the diameters of the vortex structures and provides estimates of the accuracy of the calculated data.

A graph of the distribution of the relative values of the static pressure over the surface of the tandem step model is shown in Fig. 34. The calculation was carried out using the SA turbulence model. The SD

Table 22. FlowVision calculation of flow separation and attachment points

	Exp.	Calc. SA	SA δ, %
Separation *S*	0.1 *h*	0.17 *h*	δ% = 4
Attachment *R*	1.85 *h*	2.57 *h*	δ% = 41

Table 23. Calculation of FlowVision points on the zero velocity line (*Y* coordinates)

X	Exp. (*Y*)	Calc. SA (*Y*)	SA δ_Y, %
0.35	–0.32 *h*	–0.28 *h*	12.5
0.63	–0.53 *h*	–0.45 *h*	15
0.94	–0.71 *h*	–0.63 *h*	11

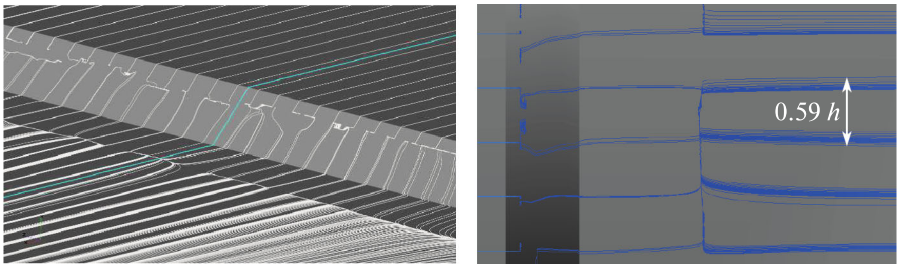

Fig. 33. FlowVision calculation of limit streamlines on the tandem surface steps.

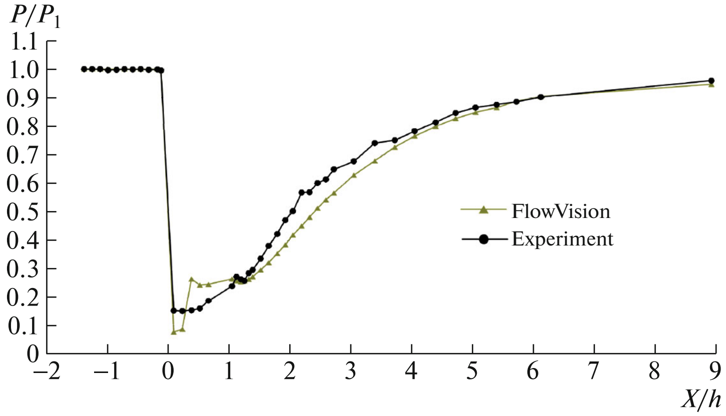

Fig. 34. FlowVision calculation of static pressure on the surface of a tandem step.

of the calculated and experimental pressure values obtained using the SA turbulence model is presented in Table 25.

A significant difference between the calculated and experimental data is observed at the rarefaction stage ($x/h = 0.02–1.0$) and in the flow compression section ($x/h = 1.0–4.0$).

Diagrams of relative Pitot pressure values plotted along the *Y* coordinate are shown in four sections; see Fig. 35. The SD of the calculated and experimental Pitot pressure values is given in Table 26.

The maximum differences between the calculated and experimental data are observed in sections 1, 3, and 4 and are of a shear nature.

Table 24. FlowVision calculation of characteristic sizes of vortex structures

	Exp.	Calc. SA	SA δ_D, %
Size of vortex structures	0.53 *h*	0.59 *h*	11

Table 25. SD of static pressure values in FlowVision calculations

Turbulence model	SA
Δ	0.0510

Table 26. SD from experimental Pitot pressure values in FlowVision calculations

X	−5.22 *h*	0.35 *h*	0.64 *h*	5.22 *h*
ΔSST	0.0653	0.0167	0.0413	0.0671

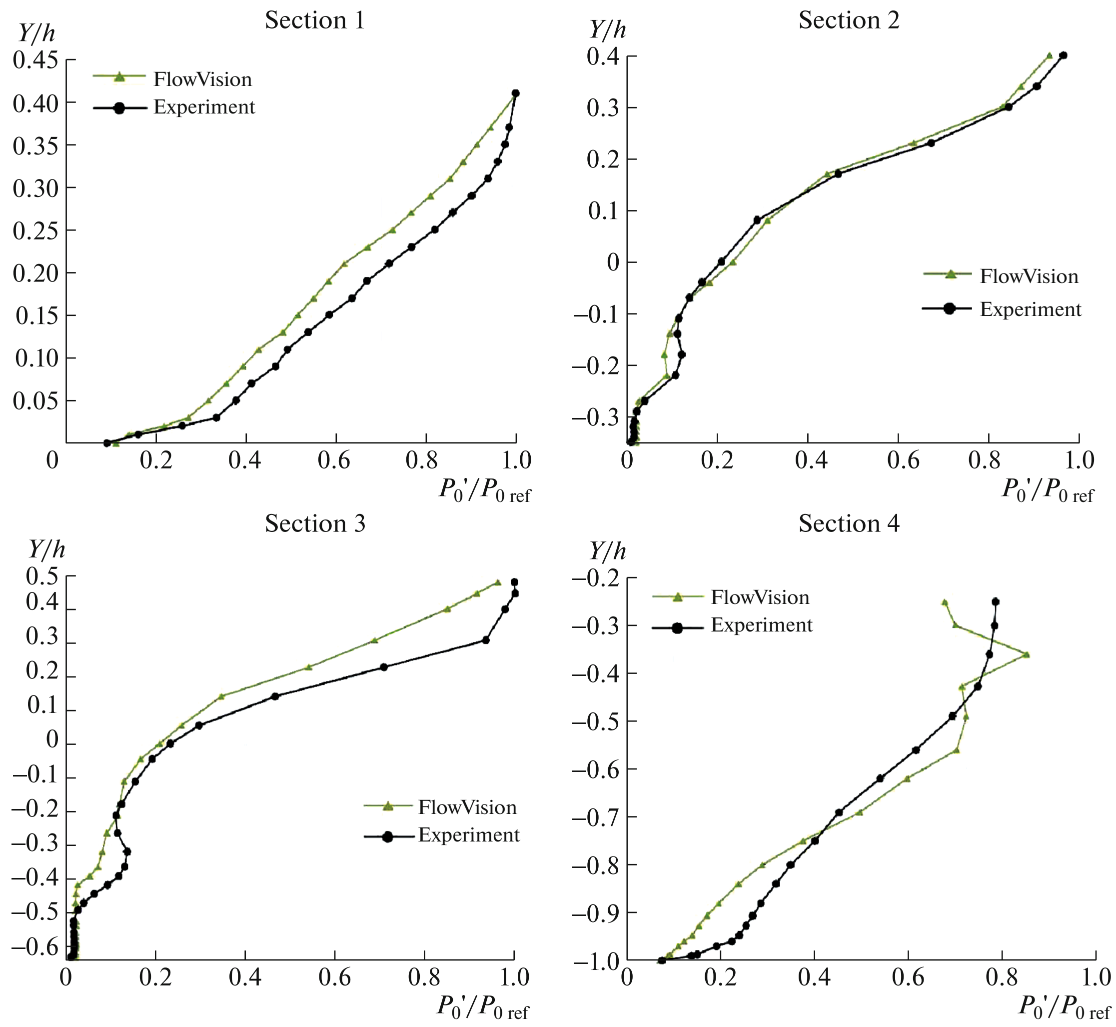

Fig. 35. Calculation of FlowVision Pitot pressure diagrams in given sections.

10. TEST CALCULATION USING ZHUKOVSKY TsAGI'S EWT SOFTWARE

The TsAGI EWT calculation code [27] is a standard software product designed to solve problems of internal and external aerodynamics. This code uses finite volume methods to solve gas dynamics equations on structured grids. In this study, a vortex-resolving algorithm for solving the Navier–Stokes equations is used, which is constructed using the hybrid RANS-LES approach of IDDES [28]. The RANS solution was specified as the initial field. At the external boundaries, the Riemann condition for the weak reflection of disturbances was realized. At the input boundary, the condition of supersonic inflow was set, and at the output boundary, a supersonic outflow was imposed in all areas, including the boundary layer. The system of equations is closed by the DRSM turbulence model [29, 30]. On the surface of the body, all turbulent stresses were set to zero. At the input boundary, the diagonal terms of the stress tensor are $2k/3$ (k is the kinetic energy of turbulence), and the off-diagonal terms are zero. The DRSM IDDES approach was implemented for the first time and published in [31, 32]. Calculations were performed using the WENO5 hybrid scheme-CD2 with a transient function [33]. The method uses the subgrid length scale SLA [34]. Integration over time is carried out using an implicit scheme of the third order of accuracy. The transition to the LES mode in the boundary layer occurred naturally (without using a synthetic turbulence generator) at a significant distance from the step's rarefaction angle ($X = 0$).

Figure 36 shows the fragment of the computational grid used to simulate the flow in this test. The drawing is prepared in a two-dimensional approximation, which corresponds to the plane of symmetry of the model. The entrance and upper boundaries were located at a distance of 0.4 m (26 h); and output, 0.3 m (20 h). On hard surfaces, the condition was set for adhesion to a thermally insulated wall. In the transverse

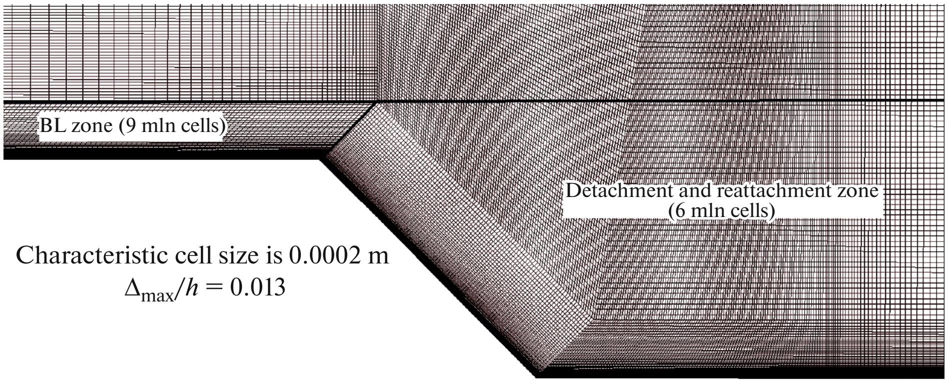

Fig. 36. Fragment of a computational grid for calculations using EWT.

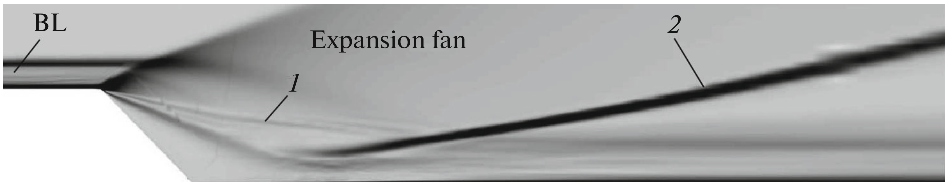

Fig. 37. Calculation of EWT flow pattern around tandem steps.

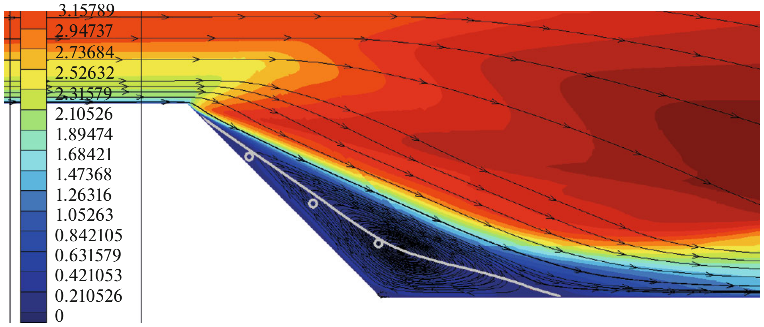

Fig. 38. Calculation of EWT fields of Mach numbers and streamlines in the separation zone.

direction, where the periodicity conditions were imposed on the boundaries, the size of the computational domain was 0.02 m (1.33 *h*). The first near-wall grid step was chosen from the condition $y^+ \le 1$, necessary for setting the adhesion conditions. The characteristic largest cell size in the boundary layer and in the separation zone is 0.0002 m (0.013*h*). The final size of the three-dimensional structured computational grid was 21 million nodes.

The length of the plate in front of the step was chosen so that the thickness of the boundary layer in the RANS calculation in the first (control) section practically coincided with the experimental value. The calculation was carried out until the moment when a quasi-periodic nonstationary process (LES mode) appeared. Then the flow averaging mode was turned on (the stage of collecting statistical data) and obtaining the correlational characteristics of turbulence. Below the averaged data are given.

Figure 37 shows the shadow pattern of the flow. Visually, it is practically no different from the experimental image (see Fig. 6). Both images highlight the main features of the flow, such as the RWF, the main shock wave *2*, and the separation shock wave *1*. The values of the flow separation and attachment points on the model surface (the *X* coordinate) are given in Table 27.

Figure 38 shows the Mach number fields and streamlines visualizing the return flow zone. The white markers indicate the position of the zero velocity line inside the separation zone. Table 28 contains the

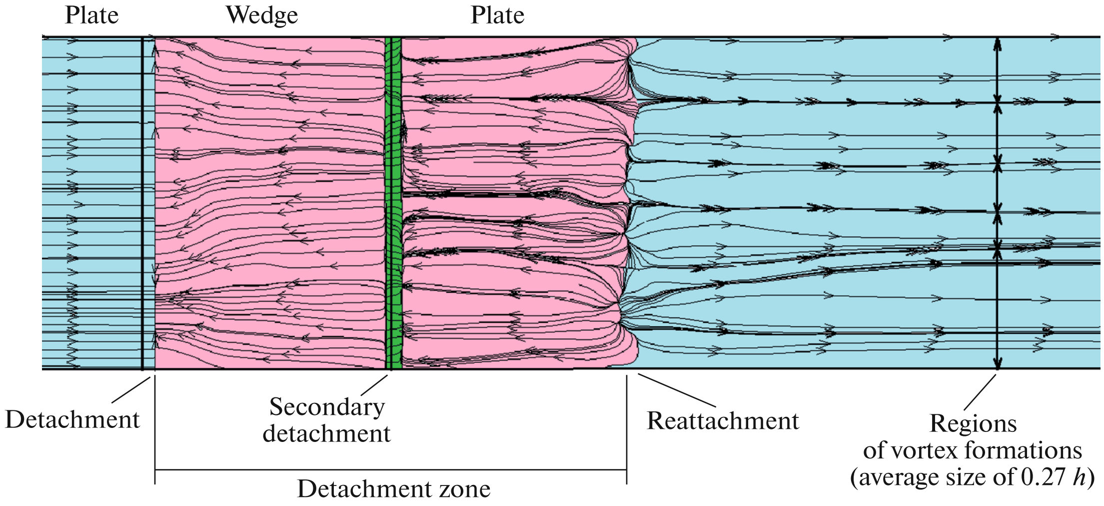

Fig. 39. Calculation of EWT limit streamlines on the surface of tandem steps.

relative coordinates of the indicated markers for the experiment and calculation and provides estimates of the calculation accuracy.

Figure 39 shows the picture of the limiting streamlines on the surface of the tandem steps and gives an estimate of the size of vortex structures such as Görtler vortices. Table 29 compares the calculated and experimental data.

In the calculation, a secondary separation is observed in the compression angle (see Fig. 39). A similar phenomenon is observed in the experiment; see Fig. 4. The average transverse size of the vortex structures in the calculation was calculated by dividing the width of the calculation zone by the number of spreading points. It can be seen that the streamlines in Fig. 39 are not parallel. Therefore, the local sizes of vortex structures varied in the range of values from 0.27 *h* up to 0.5 *h*. At a significant distance downstream, visually the distance between the flow lines leveled off and approached a size of the order of 0.5 *h*. In the experiment, the diameters of the vortices also had a fairly large scatter over the span of the model. The size of the Görtler vortex given in the experimental report was apparently the result of averaging; see Fig. 4.

A graph of the distribution of the relative values of static pressure over the surface of the tandem step model is shown in Fig. 40. The calculation was carried out using the DRSM turbulence model using the IDDES method.

Table 27. Calculation of EWT points of flow separation and attachment

	Exp.	Calc. DRSM IDDES	δ, %
Separation *S*	0.1 *h*	0.05 *h*	$\delta_S = 3$
Attachment *R*	1.85 *h*	1.95 *h*	$\delta_R = 5.7$

Table 28. Calculation of EWT points on the zero velocity line (*Y* coordinates)

X	Exp. (*Y*)	Calc. DRSM IDDES (*Y*)	δ_Y, %
0.35	–0.32 *h*	–0.26 *h*	19
0.63	–0.53 *h*	–0.45 *h*	15
0.94	–0.71 *h*	–0.67 *h*	6

Table 29. EWT calculation of characteristic sizes of vortex structures

Exp.	Calc. DRSM IDDES	SA δ_D, %
0.53 *h*	0.5 *h*	6

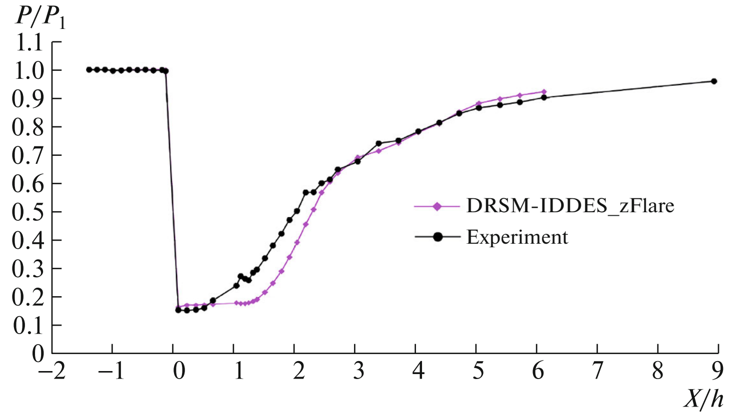

Fig. 40. Calculation of EWT static pressure on the surface of tandem steps.

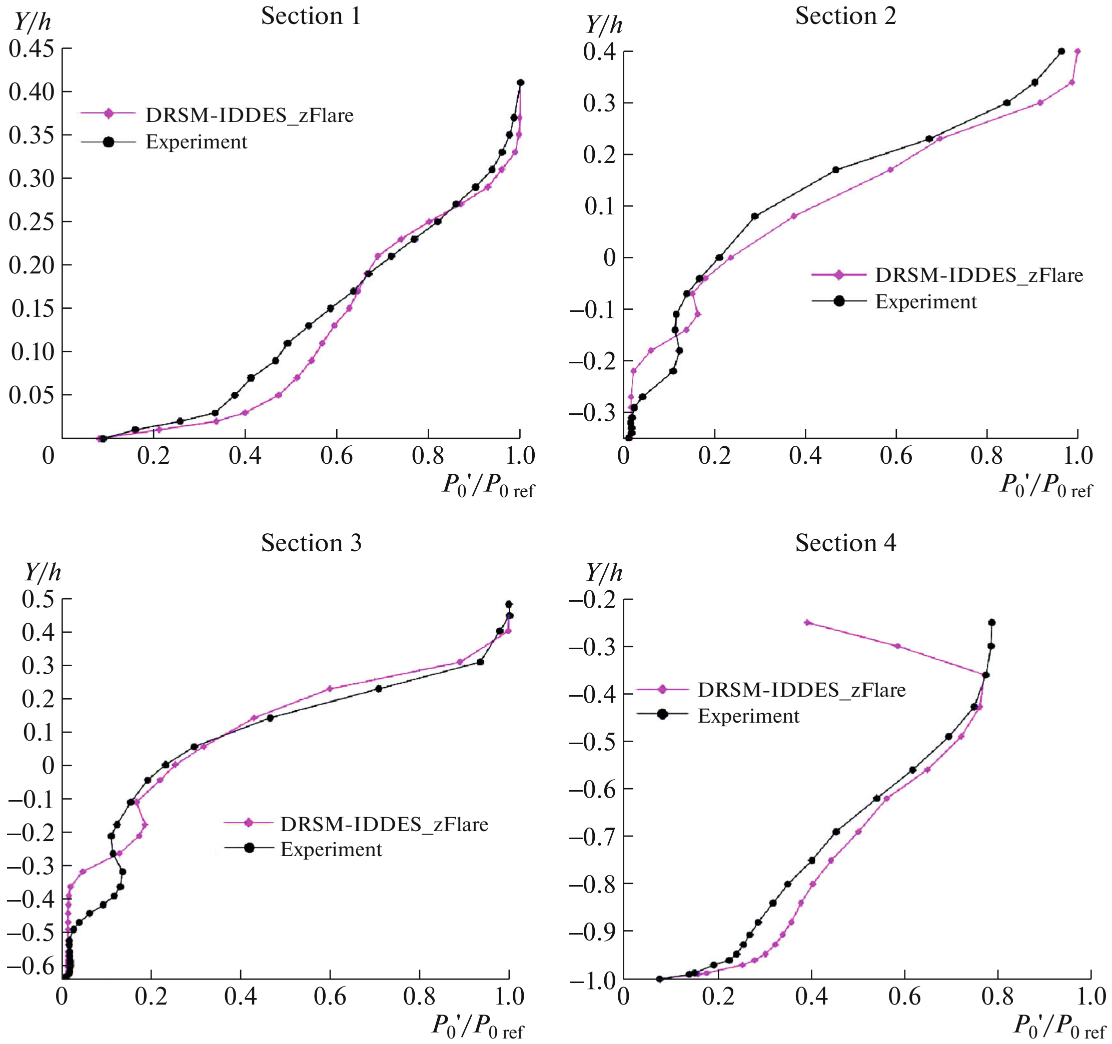

Fig. 41. Calculation of EWT Pitot pressure diagrams in given sections.

The SD of the calculated and experimental pressure values is presented in Table 30. A significant difference between the calculated and experimental data is observed at the compression stage ($x/h = 1.0–3.0$).

Diagrams of relative Pitot pressure values plotted along the Y coordinate are shown in four sections; see Fig. 41. The SD of the calculated and experimental Pitot pressure values is given in Table 31.

Table 30. SD of static pressure values in EWT calculation

Turbulence model	DRSM IDDES
Δ	0.0625

Table 31. SD from experimental Pitot pressure values in EWT calculation

X	$-5.22\,h$	$0.35\,h$	$0.64\,h$	$5.22\,h$
ΔIDDES DRSM	0.0493	0.0508	0.0459	0.1083

The maximum difference between the calculated and experimental data is observed in sections 2 and 3 and indicates that in the calculation the zone of separated (low-speed) flow occupies a larger space in height than in the experiment.

11. SUMMARY OF TEST RESULTS

To assess the accuracy of the results obtained using the tested programs, it is necessary to be tied to the solution of specific problems and use existing technical regulations. In this case, we can use an analogy with the accuracy class of the measuring sensors. This may serve as a research subject for our next work. In this article, the authors have limited themselves to a mechanical comparison of the test results, remaining within the framework of the terms “better—worse.” Table 32 summarizes these estimates of accuracy by SD and indicates the positions with the smallest and largest deviations of the calculated and experimental data. Based on the specified criteria, the Fluent SA-R program showed the best result in terms of SD.

In this case, a reasonable structure inside the separation, close to the experiment, was obtained by using the IDDES method. In general, the advantage of methods of this type becomes noticeable in problems where the spectra and inhomogeneities of turbulence, sound emission, and dynamic loads on the surface are studied.

It is of interest to compare the graphs obtained by methods of the same class. Figure 42 summarizes the results of calculating the static pressure distributions obtained using IDDES eddy-resolving methods. It is interesting to note that the influence of the turbulence model (SA and SST) on the result within NOISEtte is negligible compared to the difference from DRSM IDDES (EWT), for which the computational grid was fundamentally different. This indirectly indicates the strong grid dependence of the IDDES method. Most likely, the grid used for DRSM IDDES was not sufficient to obtain a high-quality solution, especially in the region of separation.

Table 32. Summary table of SD values

	$P(x)$	Pitot sec. 1	Pitot sec. 2	Pitot sec. 3	Pitot sec. 4
NOISEtte IDDES SA	0.0229	0.1005	0.0405	0.0674	0.0692
NOISEtte IDDES SST*	***0.0219***[1]	0.1108[2]	0.0384	0.0693[2]	0.0716
EWT IDDES DRSM	0.0625	0.0493	0.0508	0.0459	0.1083[2]
GRAT-SST	0.0315	0.0387	0.0507	0.0296	0.0524
LOGOS SA-R	0.0546	0.0783	0.0697[2]	0.0295	0.1051
FlowVision SA	0.0510	0.0653	***0.0167***[1]	0.0413	0.0671
Fluent SA	0.0530	0.0281	0.0234	0.0281	0.0530
Fluent SST	0.0920[2]	0.0328	0.0385	0.0328	0.1079
Fluent SA-RC**	0.0460	***0.0258***[1]	0.0211	***0.0258***[1]	***0.0455***[1]
Fluent SST-RC	0.0880	0.0312	0.0376	0.0312	0.1043

Index 1 (bold italic), smallest SD.
Index 2 (underlining), highest SD.
* The largest number of largest SDs.
** The largest number of smallest SDs.

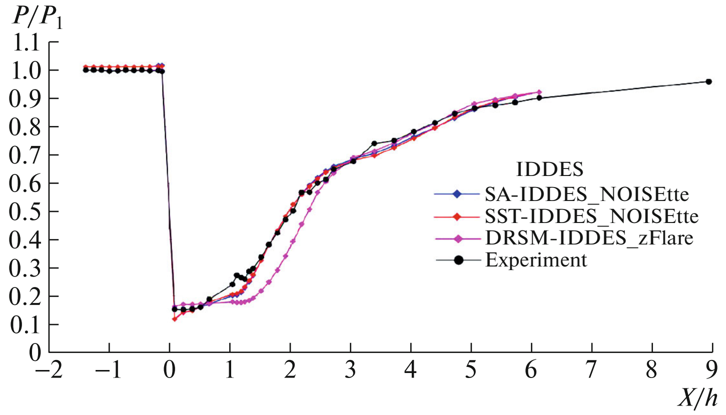

Fig. 42. Calculation of static pressure on the surface of steps using IDDES methods.

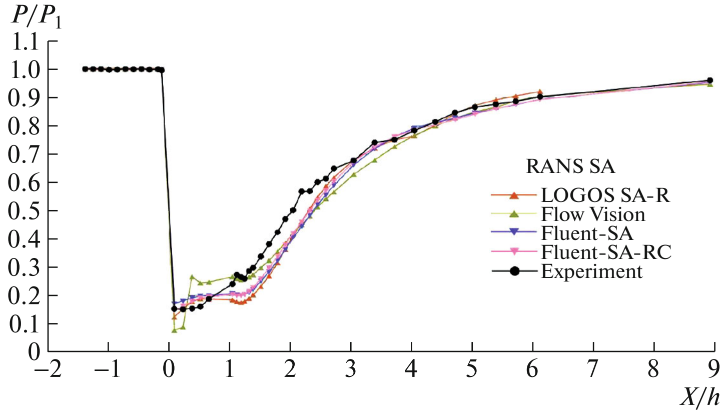

Fig. 43. Calculation by RANS SA methods of static pressure on the surface of steps.

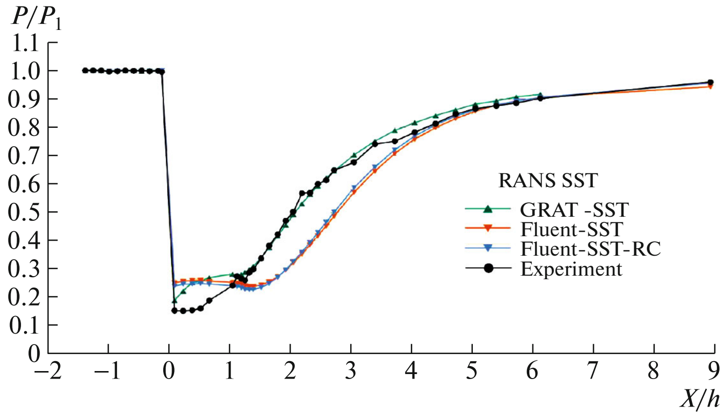

Fig. 44. Calculation by RANS SST methods of static pressure on the surface of steps.

Figure 43 summarizes the results obtained within the RANS approach using different versions of the SA turbulence model.

The comparison allows us to state that all the tested codes give similar results. Moreover, the difference between different programs is several times smaller than the difference between calculation and experiment. The biggest questions regarding the accuracy of calculations on the rarefaction step ($1.0 > x/h > 0$) arise in relation to FlowVision, which gives difficult-to-explain overshoots of the solution.

Figure 44 presents the summary results obtained from the RANS approach using different versions of the SST turbulence model.

It should be noted that there is a noticeable difference in the results obtained using Fluent and GRAT, which may be a consequence of differences in the types of grids or differences in the setup of the turbulence model (GRAT). All of the above programs give noticeable errors on the rarefication step ($1.0 > x/h > 0.0$). At the same time, Fluent does not significantly extend the level of rarefaction obtained in the experiment. Note that calculations with Fluent SA and Fluent SST were performed on the same grid. Consequently, the insufficient level of the flow's rarefaction obtained with Fluent SST is not a consequence of the roughness of the computational grid, but is explained by the peculiarities of the SST turbulence model.

CONCLUSIONS

1. A comparison of the calculated data obtained by various methods with the results of a test experiment shows that all the methods used reliably model the physical features of the flow near the surface of a tandem of 3D back-forcing and forward-forcing steps. Nevertheless, there is no reason to assert that a good resolution of the calculated data has been obtained, since the noted deviations of the calculation from the experiment are multidirectional and depend on various factors, such as the implementation of the calculation method, the turbulence model, and the quality of the computational grid.

2. The presented data have the necessary completeness and allow us to reasonably select one of the tested methods for solving specific problems with an assessment of the accuracy of the results obtained.

3. This study should be continued by achieving grid convergence and eliminating the grid factor from the analysis of the performance of turbulence models.

FUNDING

This work was supported by ongoing institutional funding. No additional grants to carry out or direct this particular research were obtained.

CONFLICT OF INTEREST

The authors of this work declare that they have no conflicts of interest.

REFERENCES

1. A. A. Zheltovodov, L. Ch.-Yu. Mekler, and E. Kh. Shilein, "Peculiarities of development of separated flows at compression corners behind expansion waves," Preprint No. 10 (Khristianovich Inst. of Theoretical and Applied Mechanics, Sib. Branch, Russ. Acad. Sci., Novosibirsk, 1987).
2. S. M. Bosnyakov, A. P. Duben, A. A. Zheltovodov, T. K. Kozubskaya, S. V. Matyash, and S. V. Mikhailov, "Numerical simulation of supersonic separated flow over inclined backward-facing step using RANS and LES methods," Math. Models Comput. Simul. **12**, 453–463 (2020). https://doi.org/10.1134/s2070048220040043
3. J. Fang, Yu. Yao, A. A. Zheltovodov, Z. Li, and L. Lu, "Direct numerical simulation of supersonic turbulent flows around a tandem expansion-compression corner," Phys. Fluids **27**, 125104 (2015). https://doi.org/10.1063/1.4936576
4. A. A. Babulin, S. M. Bosnyakov, V. V. Vlasenko, M. F. Engulatova, S. V. Matyash, and S. V. Mikhailov, "Experience of validation and tuning of turbulence models as applied to the problem of boundary layer separation on a finite-width wedge," Comput. Math. Math. Phys. **56**, 1020–1033 (2016). https://doi.org/10.1134/s0965542516060051
5. I. I. Volonikhin, V. D. Grigor'ev, V. S. Dem'yanenko, K. I. Pisarenko, and A. M. Kharitonov, "Supersonic aerodynamic tube T-313," in *Collection of Sci. Papers of the Khristianovich Inst. of Theoretical and Applied Mechanics, Sib. Branch, USSR Acad. Sci.: Aerophysical Studies* (Novosibirsk, 1972), pp. 8–11.
6. I. V. Abalakin, P. A. Bakhvalov, A. V. Gorobets, A. P. Duben', and T. K. Kozubskaya, "Parallel software package NOISEtte for large-scale computation of aerodynamic and aeroacoustic applications," Vychisl. Metody Program. **13** (3), 110–125 (2012).
7. E. K. Guseva, A. V. Garbaruk, and M. Kh. Strelets, "Assessment of delayed DES and improved delayed DES combined with a shear-layer-adapted subgrid length-scale in separated flows," Flow, Turbul. Combust. **98**, 481–502 (2017). https://doi.org/10.1007/s10494-016-9769-7
8. P. R. Spalart and S. R. Allmaras, "A one-equation turbulence model for aerodynamic flows," Rech. Aerospatiale, No. 1, 5–21 (1994).
9. F. R. Menter, M. Kuntz, and R. Langtry, "Ten years of industrial experience with the SST turbulence model," Turbul., Heat Mass Transfer **4**, 625–632 (2003).

10. A. P. Duben and T. K. Kozubskaya, “Evaluation of quasi-one-dimensional unstructured method for jet noise prediction,” AIAA J. **57**, 5142–5155 (2019).
https://doi.org/10.2514/1.j058162

11. I. Abalakin, P. Bakhvalov, and T. Kozubskaya, “Edge-based reconstruction schemes for unstructured tetrahedral meshes,” Int. J. Numer. Methods Fluids **81**, 331–356 (2016).
https://doi.org/10.1002/fld.4187

12. P. Bakhvalov and T. Kozubskaya, “EBR-WENO scheme for solving gas dynamics problems with discontinuities on unstructured meshes,” Comput. Fluids **157**, 312–324 (2017).
https://doi.org/10.1016/j.compfluid.2017.09.004

13. M. L. Shur, P. R. Spalart, M. K. Strelets, and A. K. Travin, “Synthetic turbulence generators for RANS-LES interfaces in zonal simulations of aerodynamic and aeroacoustic problems,” Flow, Turbul. Combust. **93**, 63–92 (2014).
https://doi.org/10.1007/s10494-014-9534-8

14. A. V. Struchkov, A. S. Kozelkov, K. N. Volkov, A. A. Kurkin, R. N. Zhuckov, and A. V. Sarazov, “Numerical simulation of aerodynamic problems based on adaptive mesh refinement method,” Acta Astronaut. **172**, 7–15 (2020).
https://doi.org/10.1016/j.actaastro.2020.03.019

15. Yu. N. Deryugin, A. V. Sarazov, and R. N. Zhuchkov, “Specific features of the Chimera calculation methodology implemented for unstructured grids,” Math. Models Comput. Simul. **9** (5), 587–597 (2017).
https://doi.org/10.1134/S2070048217050040

16. *Digital Technologies in Lifecycle of Russian Aviation: Monograph*, Ed. by M. A. Pogosyan (Mosk. Aviats. Inst., Moscow, 2020).

17. Yu. N. Deryugin, R. N. Zhuchkov, D. K. Zelenskiy, A. S. Kozelkov, A. V. Sarazov, N. F. Kudimov, Yu. M. Lipnickiy, A. V. Panasenko, and A. V. Safronov, “Validation results for the LOGOS multifunction software package in solving problems of aerodynamics and gas dynamics for the lift-off and injection of launch vehicles,” Math. Models Comput. Simul. **7**, 144–153 (2015).
https://doi.org/10.1134/S2070048215020052

18. J. Dacles-Mariani, G. G. Zilliac, J. S. Chow, and P. Bradshaw, “Numerical/experimental study of a wingtip vortex in the near field,” AIAA J. **33**, 1561–1568 (1995).
https://doi.org/10.2514/3.12826

19. D. N. Smolkina, O. N. Borisenko, M. V. Cherenkova, A. G. Giniyatullina, M. V. Kuz’menko, N. V. Chukhmanov, E. V. Potekhina, N. V. Popova, and M. R. Turusov, “An automatic generator of unstructured polyhedral grids in the LOGOS software preprocessor,” Vopr. At. Nauki Tekh., Ser.: Mat. Model. Fiz. Protsessov, No. 2, 25–39 (2018).

20. O. A. Bessonov and N. A. Kharchenko, “Software platform for supercomputer modeling of aerothermodynamics problems,” Programmnaya Ingeneria **12**, 302–310 (2021).
https://doi.org/10.17587/prin.12.302-310

21. N. A. Kharchenko and M. A. Kotov, “Aerothermodynamics of the Apollo-4 spacecraft at earth atmosphere conditions with speed more than 10 km/s,” J. Phys.: Conf. Ser. **1250**, 012012 (2019).
https://doi.org/10.1088/1742-6596/1250/1/012012

22. N. A. Kharchenko and N. A. Nosenko, “Numerical simulation of high-speed flow around a cylindrical-conical body and a double cone,” Matematicheskoe Model. Chislennye Metody, No. 3, 33–46 (2022).
https://doi.org/10.18698/2309-3684-2022-3346

23. *ANSYS Fluent User’s Guide, Release 2021 R1* (ANSYS, 2021).

24. M. L. Shur, M. K. Strelets, A. K. Travin, and P. R. Spalart, “Turbulence modeling in rotating and curved channels: Assessing the Spalart-Shur correction,” AIAA J. **38**, 784–792 (2000).
https://doi.org/10.2514/3.14481

25. P. E. Smirnov and F. R. Menter, “Sensitization of the SST turbulence model to rotation and curvature by applying the Spalart-Shur correction term,” in *ASME Turbo Expo 2008: Power for Land, Sea, and Air: Volume 6: Turbomachinery, Parts A, B, and C* (ASMEDC, Berlin, 2008), pp. GT2008–50480.
https://doi.org/10.1115/gt2008-50480

26. *FlowVision: User’s Guide, Version 3.12.05* (TESIS, Moscow, 2021).
https://doi.org/10.31166/voprosyistorii202104statyi18

27. *Practical Aspects of Solving the Problems of Inner and Outer Aerodynamics Using the ZEUS Technology within the EWT-TsAGI Packages: Coll. of Sci. Papers*, Trudy TsAGI, Vol. 2735 (2015).

28. A. V. Garbaruk, M. Kh. Strelets, A. K. Travin, and M. L. Shur, Modern Approaches to Modeling of Turbulence (Izd-vo Politekhnicheskogo Universiteta, St. Petersburg, 2016).

29. R.-D. Cécora, B. Eisfeld, A. Probst, S. Crippa, and R. Radespiel, "Differential Reynolds stress modeling for aeronautics," in *50th AIAA Aerospace Sciences Meeting including the New Horizons Forum and Aerospace Exposition* (American Institute of Aeronautics and Astronautics, 2012), p. 2012-0465. https://doi.org/10.2514/6.2012-465
30. R.-D. Cécora, R. Radespiel, B. Eisfeld, and A. Probst, "Differential Reynolds-stress modeling for aeronautics," AIAA J. **53**, 739–755 (2015). https://doi.org/10.2514/1.j053250
31. S. Bakhne, A. V. Volkov, I. S. Matyash, S. V. Matyash, and A. I. Troshin, "Method for calculating separated flows of the IDDES class based on DRSM turbulence model," in *Proc. 26th Workshop with Int. Participation on Jet, Separated, and Nonstationary Flows* (St. Petersburg, 2022).
32. S. Bakhne, A. V. Volkov, I. S. Matyash, S. V. Matyash, and A. I. Troshin, "Testing the method for calculating the separated flows based on the IDDES approach and DRSM turbulence model," in *Collection of Abstracts on Computational Experiment in Aeroacoustic and Aerodynamics* (Svetlogorsk, Kaliningrad oblast, 2022).
33. E. K. Guseva, A. V. Garbaruk, and M. K. Strelets, "An automatic hybrid numerical scheme for global RANS-LES approaches," J. Phys.: Conf. Ser. **929**, 012099 (2017). https://doi.org/10.1088/1742-6596/929/1/012099
34. M. L. Shur, P. R. Spalart, M. Kh. Strelets, and A. K. Travin, "An enhanced version of DES with rapid transition from RANS to LES in separated flows," Flow, Turbul. Combust. **95**, 709–737 (2015). https://doi.org/10.1007/s10494-015-9618-0